



HAL
open science

Vlasov-Poisson in 1D: waterbags

Stéphane Colombi, Jihad Touma

► **To cite this version:**

Stéphane Colombi, Jihad Touma. Vlasov-Poisson in 1D: waterbags. Monthly Notices of the Royal Astronomical Society, 2014, 441, pp.2414-2432. 10.1093/mnras/stu739 . insu-03645363

HAL Id: insu-03645363

<https://insu.hal.science/insu-03645363>

Submitted on 24 Apr 2022

HAL is a multi-disciplinary open access archive for the deposit and dissemination of scientific research documents, whether they are published or not. The documents may come from teaching and research institutions in France or abroad, or from public or private research centers.

L'archive ouverte pluridisciplinaire **HAL**, est destinée au dépôt et à la diffusion de documents scientifiques de niveau recherche, publiés ou non, émanant des établissements d'enseignement et de recherche français ou étrangers, des laboratoires publics ou privés.

Vlasov–Poisson in 1D: waterbags

Stéphane Colombi^{1★} and Jihad Touma²

¹*Institut d’Astrophysique de Paris, CNRS UMR 7095 and UPMC, 98bis, bd Arago, F-75014 Paris, France*

²*Department of Physics, American University of Beirut, PO Box 11-0236, Riad El-Solh, Beirut 11097 2020, Lebanon*

Accepted 2014 April 4. Received 2014 March 12; in original form 2013 December 22

ABSTRACT

We revisit in one dimension the waterbag method to solve numerically Vlasov–Poisson equations. In this approach, the phase-space distribution function $f(x, v)$ is initially sampled by an ensemble of patches, the waterbags, where f is assumed to be constant. As a consequence of Liouville theorem, it is only needed to follow the evolution of the border of these waterbags, which can be done by employing an orientated, self-adaptive polygon tracing isocontours of f . This method, which is entropy conserving in essence, is very accurate and can trace very well non-linear instabilities as illustrated by specific examples. As an application of the method, we generate an ensemble of single-waterbag simulations with decreasing thickness to perform a convergence study to the cold case. Our measurements show that the system relaxes to a steady state where the gravitational potential profile is a power law of slowly varying index β , with β close to $3/2$ as found in the literature. However, detailed analysis of the properties of the gravitational potential shows that at the centre, $\beta > 1.54$. Moreover, our measurements are consistent with the value $\beta = 8/5 = 1.6$ that can be analytically derived by assuming that the average of the phase-space density per energy level obtained at crossing times is conserved during the mixing phase. These results are incompatible with the logarithmic slope of the projected density profile $\beta - 2 \simeq -0.47$ obtained recently by Schulz et al. using an N -body technique. This sheds again strong doubts on the capability of N -body techniques to converge to the correct steady state expected in the continuous limit.

Key words: gravitation – methods: numerical – galaxies: kinematics and dynamics – dark matter.

1 INTRODUCTION

The Vlasov–Poisson equations describe the evolution of the phase-space distribution function of a self-gravitating, collisionless system of particles in the fluid limit. In the proper units, they are given in one dimension by

$$\frac{\partial f}{\partial t} + v \frac{\partial f}{\partial v} - \frac{\partial \phi}{\partial x} \frac{\partial f}{\partial v} = 0, \quad (1)$$

$$\frac{\partial^2 \phi}{\partial x^2} = 2\rho(x, t), \quad (2)$$

$$\rho(x, t) \equiv \int f(x, v', t) dv', \quad (3)$$

where x is the position, v the velocity, t the time, $f(x, v, t)$ the phase-space density distribution function, $\phi(x, t)$ the gravitational potential and $\rho(x, t)$ the projected density.

Resolving Vlasov–Poisson equations is very challenging from the analytical point of view. The long term non-linear evolution of a

system following these equations is indeed not yet fully understood, even in the simple one-dimensional case. In general, collisionless self-gravitating systems, unless already in a stable stationary regime, are expected to evolve towards a steady state after a strong mixing phase, usually designated by *violent relaxation* (Lynden-Bell 1967). The very existence of a convergence to some equilibrium at late time through phase-mixing is however not demonstrated in the fully general case from the mathematical point of view (see, e.g., the discussion in Mouhot & Villani 2011). From the physical point of view, there is no model able to predict the exact steady profile that builds up as a function of initial conditions during their evolution. The well-known statistical theory of Lynden-Bell (1967) provides partial answers to this problem but its predictive power is limited. For instance, although it is partly successful (see, e.g., Yamaguchi 2008), it fails to reproduce in detail the steady state of many one-dimensional systems (see, e.g., Joyce & Worrakitpoonpon 2011), due to the ‘core-halo’ structure¹ that warm systems generally build

¹ We use quotes because the *core-halo* terminology is usually employed in the framework of gravothermal catastrophe while studying the thermodynamics of self-gravitating spherical systems (see, e.g., Lynden-Bell & Wood 1968).

★E-mail: colombi@iap.fr

during the course of the dynamics (see, e.g., Yamashiro, Gouda & Sakagami 1992). Some promising improvements of the Lynden-Bell theory have however been proposed to explain the structure of three-dimensional dark matter haloes (see, e.g., Hjorth & Williams 2010; Carron & Szapudi 2013; Pontzen & Governato 2013), which correspond to the case where the phase-space distribution function is initially cold. Another track relies on the derivation of solutions of the equations by conjecturing self-similarity (see, e.g., Fillmore & Goldreich 1984; Bertschinger 1985; Alard 2013). Note that assuming self-similarity is one thing, proving it is a much more challenging matter.

The only way to understand in detail how a collisionless self-gravitating system evolves according to initial conditions is therefore to resort to a numerical approach. The most widely used method by far is the N -body technique in its numerous possible implementations (see, e.g. Bertschinger 1998; Colombi 2001; Dolag et al. 2008; Dehnen & Read 2011, for reviews on the subject), where the phase-space distribution function is represented by an ensemble of macroparticles interacting with each other through softened gravitational forces. However, representing the phase-space distribution function by a set of Dirac functions can have dramatic consequences on the dynamical behaviour of the system (see, e.g., Melott et al. 1997; Melott 2007). The irregularities introduced by this discrete representation, along with N -body relaxation, can eventually drive the system far from the exact solution. For instance, in the one-dimensional case, collisional relaxation is expected to drive eventually the system in thermal equilibrium (see, e.g., Rybicki 1971), which is indeed obtained in N -body simulations after sufficient time (see, e.g., Joyce & Worrakitpoonpon 2010, and references therein). Such an equilibrium is clearly not a must in the continuous limit, where there is an infinity of stable steady states to which the system can relax (see, e.g., Chavanis 2006; Campa, Dauxois & Ruffo 2009). Such steady states, when different from thermal equilibrium, are reached at best only during a limited amount of time when using an N -body approach. Moreover, there is no guarantee that the steady solution given by the N -body simulation is the correct one.

Fortunately, there are alternatives to the N -body approach, consisting in solving numerically Vlasov–Poisson equations directly in phase-space. For instance, in plasma physics, the most-used solver is the so-called splitting algorithm of Cheng & Knorr (1976) – where the phase-space distribution function is sampled on a grid – and its numerous subsequent improvements, modifications and extensions (see, e.g., Shoucri & Gagne 1978; Sonnendrücker et al. 1999; Filbet, Sonnendrücker & Bertrand 2001; Alard & Colombi 2005; Umeda 2008; Crouseilles, Respaud & Sonnendrücker 2009; Crouseilles, Mehrenberger & Sonnendrücker 2010; Campos Pinto 2011, but this list is far from being exhaustive). In astrophysics, this method was applied successfully to one-dimensional systems (Fujiwara 1981), to axisymmetric (3D phase-space) and non-axisymmetric discs (4D phase-space; Nishida et al. 1981; Watanabe et al. 1981) and to spherical systems (3D phase-space; Fujiwara 1983). However, due to limitations of available computing resources, its implementation in full six-dimensional phase-space was achieved only very recently (Yoshikawa, Yoshida & Umemura 2013). The main drawback of Eulerian methods such as those inspired from the splitting scheme of Cheng & Knorr (1976) is to erase the fine details of the phase-space distribution at small scales as a result of coarse-graining due to finite resolution: on the long term, this coarse-graining might again lead the system far away from the exact solution. In order to fix this problem, it is possible to perform adaptive mesh refinement in phase-space (see, e.g., Alard & Colombi 2005; Mehrenberger et al. 2006; Campos Pinto 2007; Besse et al. 2008).

Another way to preserve all the details of the phase-space distribution function is to adopt a purely Lagrangian approach consisting in applying literally Liouville theorem, namely that the phase-space distribution function is conserved along trajectories of test particles as

$$f[x(t), v(t), t] = \text{constant}. \quad (4)$$

This property can indeed be exploited in a powerful way by decomposing the initial distribution on small patches, the *waterbags*, where f is approximated by a constant.² From equation (4), it follows that inside each waterbag, the value of f remains unchanged during evolution, which implies that it is only needed to resolve the evolution of the boundaries of the patches. The terminology ‘waterbag’ comes from the incompressible nature of the collisionless fluid in phase-space, which reflects the fact that the area of each patch is conserved. Therefore, their dynamics is analogous to that of an infinitely flexible bag full of water. In one dimension, the numerical implementation is therefore potentially very simple: one just needs to follow the boundaries of the waterbag with a polygon, which can be enriched with new vertices when the shape of the waterbag gets more involved.

The equation of motion of the polygon vertices is the same as test particles, where the acceleration a is given in one dimension by the difference between the total mass $M_{\text{right}}(x)$ at the right of position x and the total mass $M_{\text{left}}(x)$ at the left of x as

$$\begin{aligned} a(x, t) &= -\frac{\partial \phi}{\partial x} = M_{\text{right}}(x, t) - M_{\text{left}}(x, t) \\ &= M_{\text{tot}} - 2M_{\text{left}}(x, t) \end{aligned} \quad (5)$$

for a total mass M_{tot} . We have

$$M_{\text{left}}(x, t) = \int_{x' \leq x} dx' dv' f(x', v', t). \quad (6)$$

This can be rewritten, if f is approximated by a constant with value f_k within a patch, P_k , $k = 1, \dots, N_{\text{patch}}$, as

$$M_{\text{left}}(x, t) = \sum_{k=1}^{N_{\text{patch}}} f_k \int_{x' \leq x, (x', v') \in P_k} dx' dv'. \quad (7)$$

Application of Green’s theorem reads

$$M_{\text{left}}(x) = \sum_{k=1}^{N_{\text{patch}}} f_k \oint_{x' \leq x, \partial P_k} v(s) dx'(s), \quad (8)$$

where s is a curvilinear coordinate. This equation represents the essence of the dynamical setting of waterbag method: if one decomposes the phase-space distribution function over a number of patches where it is assumed to be constant, resolution of Poisson equation reduces to a circulation along the contours of each individual patch.

The waterbag model was introduced by DePackh (1962) and its first numerical implementation was performed in plasma physics by Roberts & Berk (1967), followed soon in the gravitational case by Janin (1971) and Cuperman, Harten & Lecar (1971a,b). We sketched a modern implementation of the algorithm in Colombi & Touma (2008) that we aim to present in detail below. Although this numerical technique was one of the pioneering methods used to solve Vlasov–Poisson equations, along with the N -body approach

² Note thus that a representation of a smooth phase-space distribution function by a stepwise distribution of waterbags remains still irregular, but obviously much less than a set of Dirac functions as in the N -body case.

(see, e.g., Hénon 1964, and references therein), it has not been used in astrophysics since the seventies, except in the cold case limit, where some developments have just started (Hahn, Abel & Kaehler 2013).

Although fairly easy to implement for low-dimensional systems, this method indeed becomes very involved in six-dimensional phase-space, as one has to model the evolution of five-dimensional hypersurfaces. In the cold case, which corresponds to the initially infinitely thin waterbag limit in velocity space, the problem reduces to following the evolution of a three-dimensional sheet in six-dimensional space and remains thus feasible. Another caveat of the waterbag method is that, due to mixing in phase-space induced by the relaxation of the system to a steady state, the waterbags get considerably elongated with time, which makes the cost of the scheme increasingly large with time. This is the price to pay for conserving entropy.

The purpose of this paper is to describe and to test thoroughly a modern numerical implementation of the waterbag method in one dimension. One goal is to prepare upcoming extensions of this method to higher number of dimensions. As part of the tests, we study in detail the evolution of single waterbags in an attempt to perform a convergence study to the cold limit, particularly relevant to cosmology in the framework of the cold dark matter paradigm. We measure the scaling behaviour of the inner part of the system. We compare it to theoretical predictions and to results obtained previously in the literature with N -body simulations.

This paper is thus organized as follows. In Section 2, we present the algorithm, of which the main ingredients were sketched briefly in Colombi & Touma (2008). The performances of the algorithm are tested thoroughly for systems with a carefully chosen set of initial conditions: an initially Gaussian $f(x, v)$, which is expected to evolve to a quasi-stationary state through quiescent mixing (Alard & Colombi 2005), an initially random set of warm haloes that will be seen, on the contrary, to develop chaos and finally, an ensemble of single-waterbag simulations, where the distribution function is initially supported by an ellipse of varying thickness. In Section 3, we examine in detail the set of single-waterbag simulations and study the properties of the system brought about by relaxation processes in the nearly cold regime. The cold limit was previously studied in detail in one dimension with exact implementations of the N -body approach (see, e.g., Binney 2004; Schulz et al. 2013). It was found in particular by Schulz et al. (2013) that the projected density relaxes to a singular profile of the form $\rho(x) \propto x^{\beta-2}$ with $\beta \simeq 1.53$. We check if this property is recovered with the waterbag technique by performing a convergence study to the cold case. Our analyses are supported by analytical calculations. Finally, Section 4 summarizes and discusses the main results of this paper. To lighten the presentation, only the most important results are presented in the core or the paper: technical details are set apart in a coherent set of extensive appendices that can be found online.

2 THE ALGORITHM

Integral (8) can be conveniently rewritten as

$$M_{\text{left}}(x) = \oint_{x' \leq x, \partial \mathcal{P}} \delta f(s) v(s) dx'(s), \quad (9)$$

$$\delta f(s) \equiv f^{\text{right}}(s) - f^{\text{left}}(s), \quad (10)$$

where $f^{\text{right}}(s)$ and $f^{\text{left}}(s)$ are the values of the phase-space distribution function when looking at the right and at the left, respectively, of the contour when facing the direction of circulation defined by

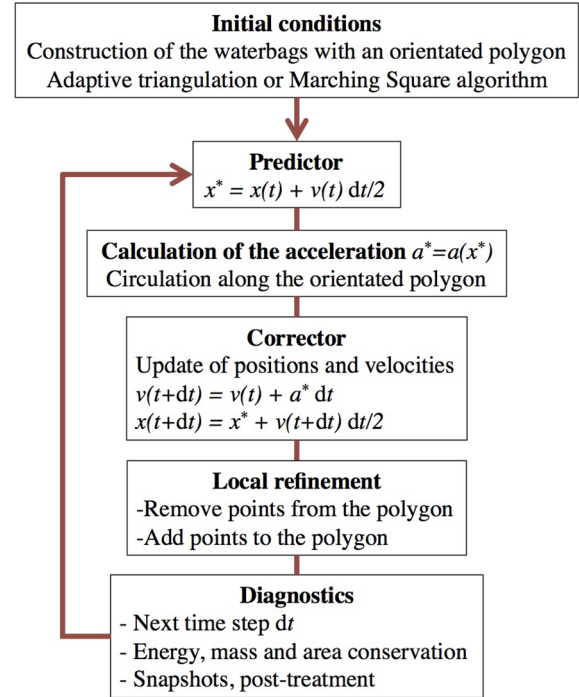


Figure 1. The main steps of our waterbag algorithm.

the curvilinear coordinate s . The global contour $\partial \mathcal{P}$ passes through a set of orientated loops (∂P_k in equation 8),³ but without repeating twice the border common to two adjacent waterbags. In practice, it is modelled with a self-adaptive orientated polygon composed of N segments joining together $N + 1$ vertices following the equations of motion.

Our algorithm is summarized in Fig. 1. Its important steps, already sketched briefly in Colombi & Touma (2008), define the structure of this section. Section 2.1 explains the way the initial phase-space distribution function is sampled with the orientated polygon, which allows us to introduce the simulations performed in this paper. Section 2.2 describes the dynamical component of the algorithm and is divided in five parts: Section 2.2.1 and 2.2.2 comment briefly on our time integration scheme and on the way we circulate along the orientated polygon to solve Poisson equation; Section 2.2.3 deals with local refinement and questions the potential virtues of unrefinement; finally, Section 2.2.4 discusses diagnostics, calculation of the value of the time step and energy conservation.

2.1 Initial condition generation and presentation of the simulations

A natural way to sample initial conditions consists in defining each waterbag as the area enclosed between two successive isocontours of the phase-space distribution function. The isocontours are chosen such as to bound the mean square difference between the true and the sampled (step-wise) phase-space distribution function weighted by the waterbag thickness, which means that local intercontour spacing roughly scales like $1/\sqrt{|\nabla f|}$ where $|\nabla f|$ is the magnitude of the gradient of the phase-space distribution function. To draw the isocontours, we use the so-called marching square algorithm, inspired

³ The connecting parts between two isocontours do not contribute to the dynamics.

from its famous three-dimensional alter-ego (Lorensen & Cline 1987). Additional technical details can be found in Appendix B.

Note that at the end of initial conditions generation, we recast coordinates in the centre-of-mass frame.⁴

Now, we introduce and comment on the three sets of simulations performed in this paper, namely an initially Gaussian $f(x, v)$ (Section 2.1.1), an ensemble of random haloes (Section 2.1.2) and single waterbags of varying thickness (Section 2.1.3). Additional details can be found in Appendix A and its Table A1, which provides the main parameters of the simulations. The large variety of these initial conditions, as shown below, should be sufficient to test thoroughly the performances of the waterbag method.

2.1.1 Gaussian initial conditions: Landau damping and importance of initial waterbag sampling

Our Gaussian initial conditions correspond to a phase-space distribution given by $f(x, v) = 4 \exp[-(x^2 + v^2)/0.08]$ smoothly truncated at $x^2 + v^2 \gtrsim 1$. The advantage of this setup is that it is not very far from the thermal equilibrium solution.⁵ The smoothness of the Gaussian function and the supposedly attractor nature of thermal equilibrium should, according to intuition, make this system quiescent. It was indeed previously shown numerically with a semi-Lagrangian solver that this system converges smoothly to a quasi-steady-state close to (but still slightly different from) thermal equilibrium (Alard & Colombi 2005). Landau damping represents in plasma physics a fundamental test bed case of Vlasov codes: our Gaussian initial conditions allow us to study the analogous of it in the gravitational case.

Fig. 2 shows the results obtained with our waterbag code for these Gaussian initial conditions. It illustrates how important is the initial condition generation step. In the first and third line of panels, function $f(x, v)$ is sampled with only 10 waterbags, while in the second and fourth line, it is sampled with 84 waterbags. Although both simulations coincide with each other at early times, a non-linear instability soon builds up in the 10-waterbags simulation, at variance with the 84 one, which remains quiescent. This is even clearer in Action–Angle coordinates, as displayed in Fig. 3: in the left-hand column of panels, the poorness of initial waterbags sampling induces some oscillations, already visible at $t = 25$, which amplify and create non-linear resonant instabilities. On the other hand, in the right-hand column of panels, the 84-waterbags simulation presents the typical signature of Landau damping. The quiescent nature of the system is also confirmed by the fact that the total vertex number and the total length of the waterbag contours augment linearly with time (see Appendix C4). Even though the instability observed in the 10-waterbags simulation might actually be present in the true system at the microscopic level, its early appearance is clearly due to the unsmooth representation of our waterbag approach. It can be delayed by augmenting the contour sampling. This effect would happen likewise in an N -body simulation (Alard & Colombi 2005).

2.1.2 Random set of warm haloes: a chaotic system

Fig. 4 shows the case of an initially random set of haloes, which represents our second test. Each halo is supposed to be at thermal equilibrium and is sampled with only three waterbags to minimize

computational cost. As shown in Appendix C4, this simulation soon builds up chaos with a Lyapunov exponent equal to 0.05 as an effect of the gravitational interaction between the haloes (this effect is dominant over other instabilities that might develop due to the contour undersampling just discussed above). This numerical experiment represents thus an important test of the accuracy of the code in rather extreme conditions, somewhat opposite to the quiescent case provided by the smooth Gaussian $f(x, v)$ of previous section.

2.1.3 Single waterbags with varying thickness: from warm to nearly cold initial conditions

The single waterbag obviously corresponds to the simplest application of the method. It was used for instance in the seminal works of Janin (1971) and Cuperman et al. (1971a,b) but also subsequently in many other studies. It represents a useful way to cover a large range of initial conditions, from warm to nearly cold. The close-to-cold case represents by itself a challenge to simulate due to the nearly singular structures that build up in configuration space during the course of dynamics.

The initial configurations we consider, abusively denoted by ‘top hat’, are such that the waterbag boundary is an ellipse:

$$x^2 + (v/\Delta p)^2 = 1, \quad (11)$$

where Δp is a parameter quantifying the initial thickness of the waterbag. Modifying Δp is equivalent to changing the initial velocity dispersion while keeping unchanged the projected initial density profile. The total mass of the system is chosen to be unity. We performed a number of simulations with a large range of values of Δp in the interval $[0.001, 1]$. For $\Delta p = 0.003$, we also performed simulations where the initial boundaries of the waterbag are perturbed randomly. The visual inspection of these simulations (Figs 6–10) will be discussed in Section 3.1.

2.2 Runtime algorithm and tests of its performances

2.2.1 Time integration

To move the sampling points of the waterbag contours, we use the classic splitting scheme of Cheng & Knorr (1976) with a slowly varying time step: our algorithm is thus equivalent to a predictor-corrector scheme, as indicated in Fig. 1. It reduces to a symplectic leap-frog’ when the time step is kept constant (see, e.g., Hockney & Eastwood 1988).

Note that at the end of time integration, we recast coordinates in the centre of mass frame.

2.2.2 Poisson equation resolution

This step, of which the technical details are given in Appendix F1, is quite simple from the conceptual point of view, since it consists in circulating along ∂P by performing a sum over the polygon edges to compute integral (9), after a preliminary sort of the vertices of the polygon. However, despite its apparent simplicity, it corresponds by far to the most costly part of the code from the computational point of view, because many segments of the polygon can contribute to the force exerted on one point of space. Note that the circulation technique used to compute the force can be generalized to the calculation of other useful quantities, such as the projected density, $\rho(x)$, the mass profile, $M_{\text{left}}(x)$, the gravitational potential, $\phi(x)$,

⁴ Explicit expressions for the centre-of-mass coordinates are given in Appendix F3.

⁵ Equation (A4).

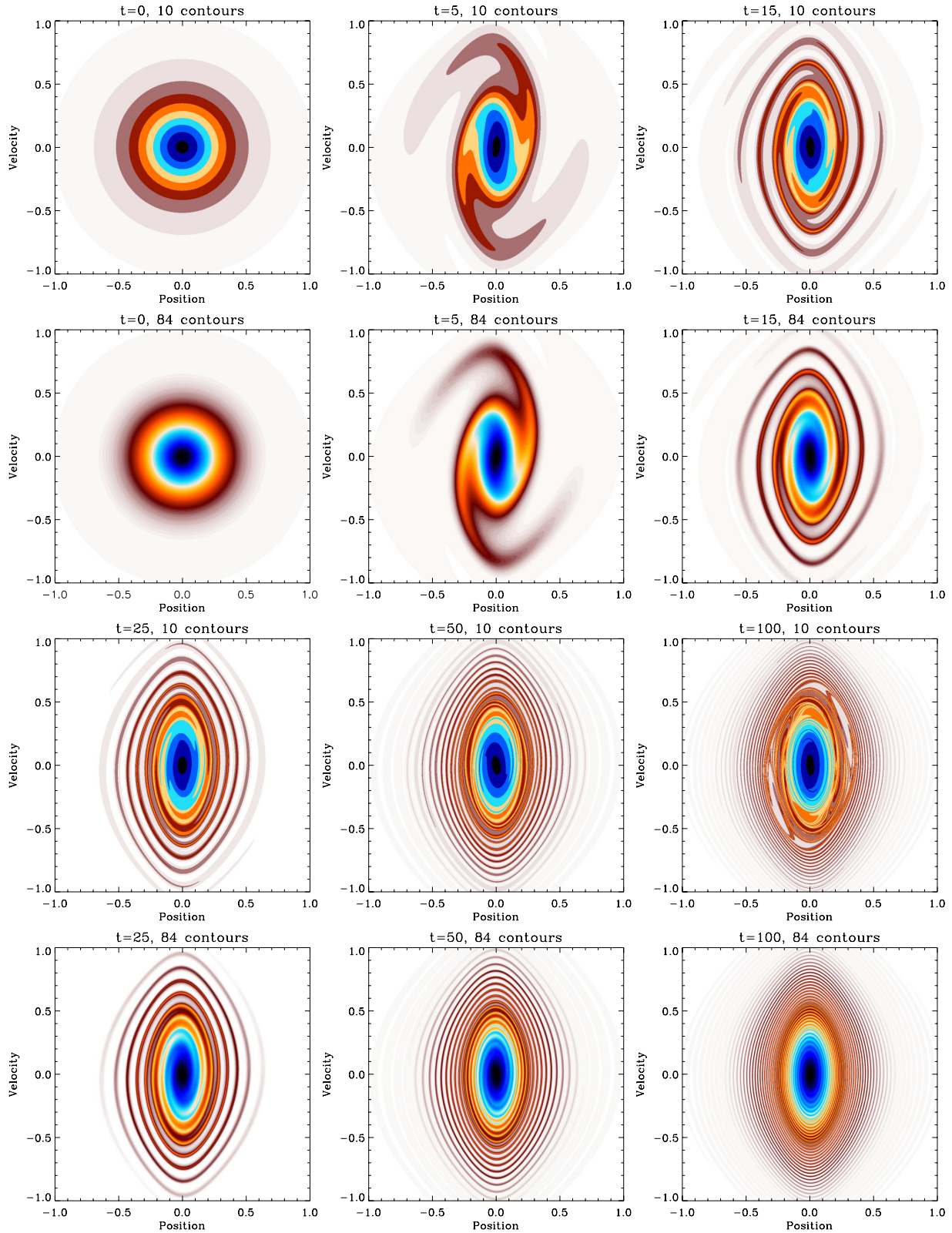


Figure 2. Simulations with Gaussian initial conditions. First and third line of panels: only 10 waterbags are used to sample initial conditions (simulation Gaussian10 in Table A1). Second and fourth line of panels: 84 waterbags are used to sample initial conditions (simulation Gaussian84 in Table A1). At early times, the two simulations agree very well with each other. At late times, an instability builds up in the 10-waterbags simulation, at variance with the 84 waterbags one which still presents the expected quiescent evolution. This numerical instability appears as well when $f(x, v)$ is represented by particles as illustrated by fig. 19 of Alard & Colombi (2005). Note that these phase-space pictures are drawn using the so-called parity algorithm described in Appendix I.

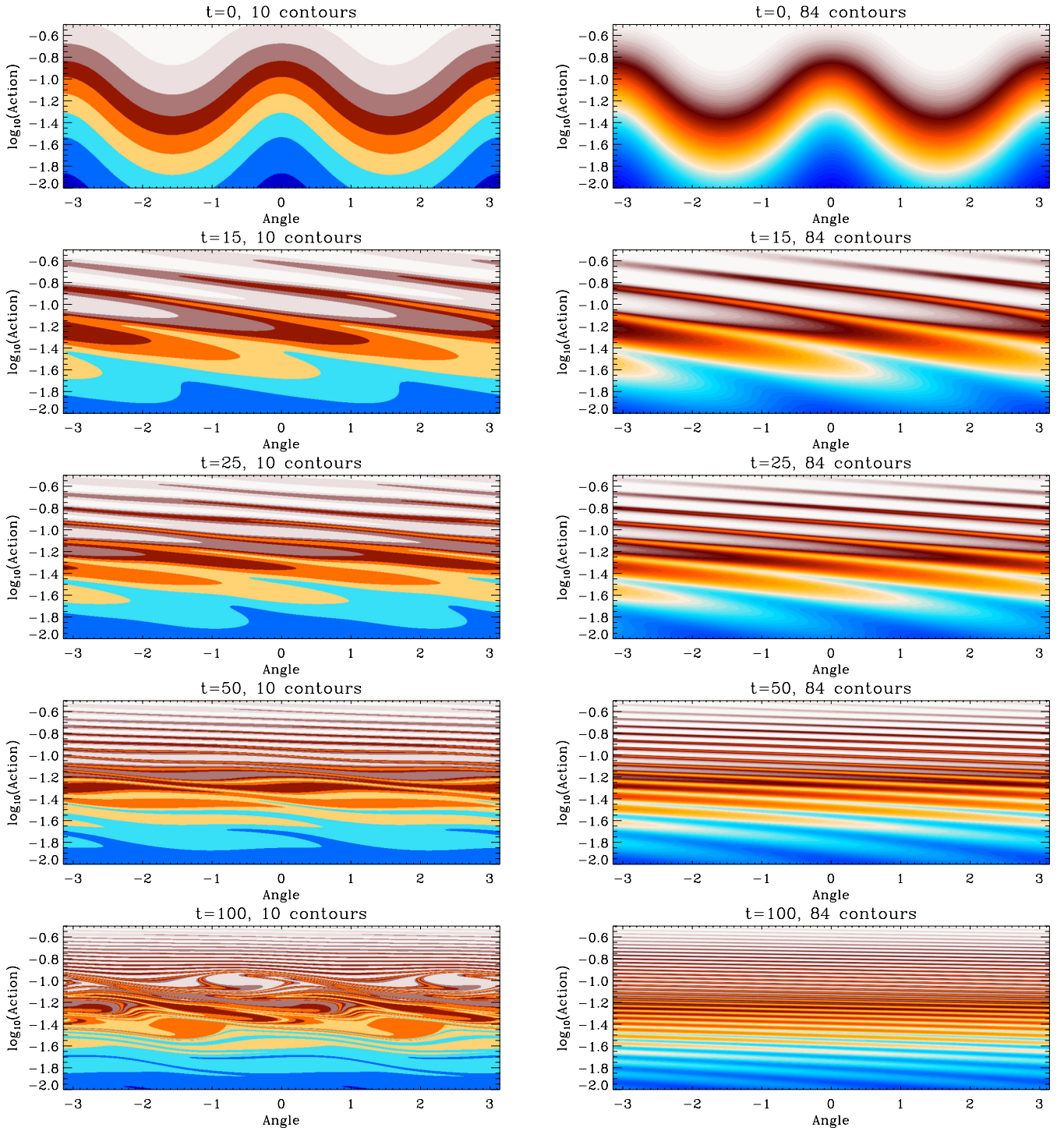


Figure 3. The simulations with Gaussian initial phase-space distribution function of Fig. 2 in Action–Angle space. The transformation from phase-space to Action–Angle space is described in Appendix G.

the bulk velocity and the local velocity dispersion, as detailed in Appendix F2.

2.2.3 Local refinement

When the shape of the waterbags contours becomes complex, it is necessary to add points to the orientated polygon to preserve all its details. Our refinement procedure is described in Fig. 5 (see also

Appendix C1). It consists of a geometric construct using arcs of circle passing through sets of three successive points of the polygon. It is equivalent, in the small angle approximation, to linearly interpolating local curvature given as the inverse of the radius of these arcs of circles. This refinement procedure is stable in the sense that it is ‘Total Variation Preserving’ in terms of the small rotations between successive segments of waterbags borders and that it makes these borders less angular (Appendix C2).

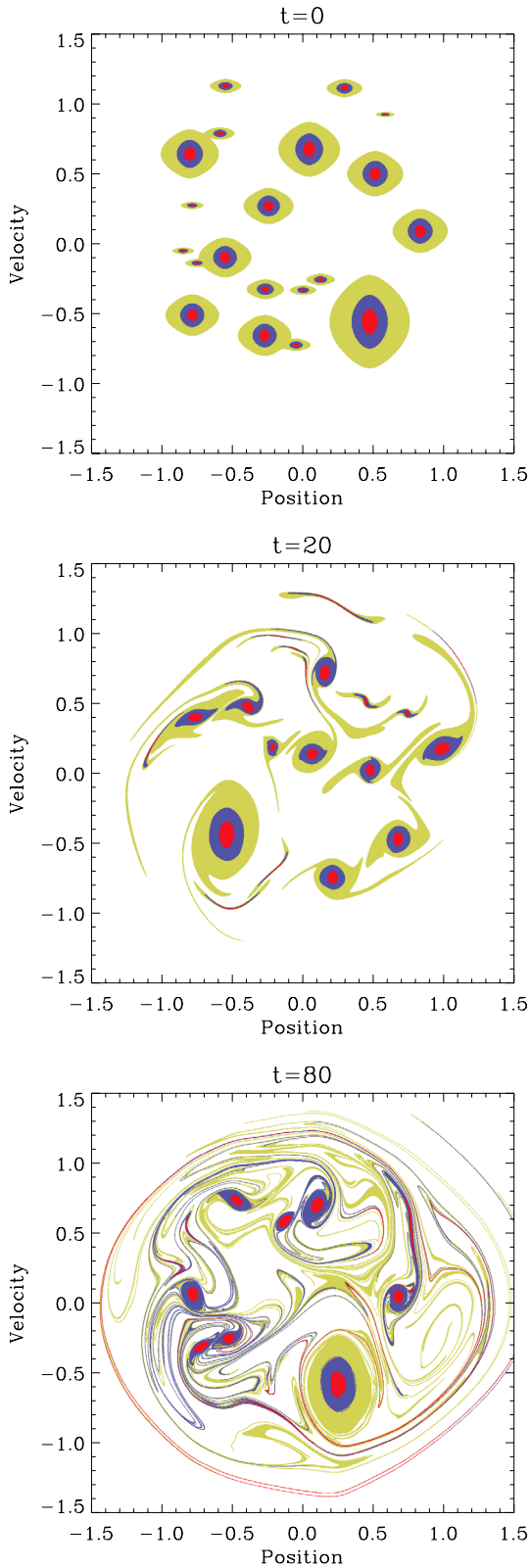


Figure 4. Evolution of an initially random set of ‘stationary’ haloes. This system develops a chaotic behaviour with a Lyapunov exponent of 0.05 as a result of the gravitational interaction between the haloes. The simulation used here corresponds to RandomU in Table A1, but other settings (RandomUT, Random and RandomUS) would look exactly the same.

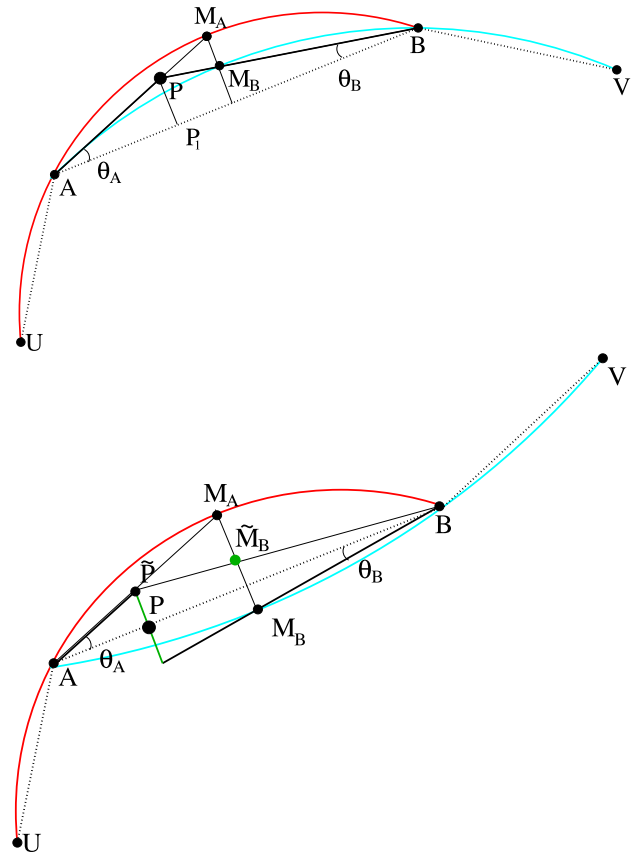


Figure 5. Interpolation method used for adding a new point P to the oriented polygon. Top panel: using, respectively, the arcs of circle $C_A = \widehat{UAB}$ of radius R_A and $C_B = \widehat{ABV}$ of radius R_B , the natural position of P would be M_A and M_B . A compromise between these two solutions is taken to be the intersection between the lines passing through segments $[A, M_A]$ and $[B, M_B]$. With this procedure, the local curvature estimated as the inverse of the radius of the arc of circle $C_P = \widehat{APB}$ is bounded by that measured at points A and B . It converges to the usual interpolation $2/R_P = 1/R_A + 1/R_B$ in the small angle approximation. Bottom panel: if there is a change in the sign of local curvature, the choice of point P is undefined. However, the smooth curve approximated by the four points U, A, B and V should intersect with segment $[A, B]$. We choose P to be at the locus of this intersection: similarly as in top panel, one computes the point \tilde{P} of intersection between the lines passing through $[A, M_A]$ and $[B, \tilde{M}_B]$, where \tilde{M}_B is symmetric to M_B with respect to the segment $[A, B]$. Then, P is just the projection of \tilde{P} on segment $[A, B]$. This procedure does not interpolate anymore local curvature in the small angle limit, but this is necessary to preserve the stability of refinement in terms of small rotations between successive segments of the waterbag borders. The panels of this figure are reprinted from Colombi & Touma (2008) with permission from Elsevier.

Refinement is performed when the variation of phase-space area S induced by adding a refinement point exceeds some threshold S_{add} or when the distance between two successive points of a contour exceeds some threshold d_{add} , e.g.

$$S(\widehat{APB}) > S_{\text{add}}, \quad (12)$$

$$d_{AB} > d_{\text{add}}, \quad (13)$$

in top panel of Fig. 5, where $S(\widehat{APB})$ is the area of the triangle \widehat{APB} and d_{AB} is the distance between A and B .⁶ The way S_{add} and d_{add} should be chosen is discussed in Appendix C3. Table A1 gives their values for the simulations we did: we have $S_{\text{add}} \in [10^{-10}, 10^{-7}]$ and $d_{\text{add}} = 0.01$ or 0.02 .

To make the algorithm more optimal, we also propose an unrefinement scheme, similarly as in Cuperman et al. (1971a): in Fig. 5, points P with

$$S(\widehat{APB}) \leq S_{\text{rem}}, \quad (14)$$

$$\min(d_{AP}, d_{PB}) \leq d_{\text{rem}} \quad (15)$$

are removed, if not violating conditions (12) and (13), of course, and if there is no local curvature sign change. In practice, $S_{\text{rem}} = S_{\text{add}}/2$ and $d_{\text{rem}} = d_{\text{add}}/2$. More technical details are given in Appendix C3.

Despite its potential virtues, same accuracy for smaller computational cost, allowing unrefinement is not optimal in our 1D case if one aims to follow a system during many dynamical times. It is indeed possible to show that vertex number dynamics changes dramatically when unrefinement is activated (Appendix C4). In particular, unrefinement is susceptible to introduce long-term noise after multiple orbital times, due to the fact that pieces of waterbag contours are alternatively refined and unrefined many times. The effects of this long-term noise can be evidenced by measurements of total energy conservation violation, as discussed below.

2.2.4 Diagnostics

Diagnostics include, of course, calculation of the value of the next time step used in the time integrator described in Section 2.2.1. To follow accurately the evolution of the system during many orbital times, we use a classic dynamical constraint on the time step modulated by two important conditions to limit excessive refinement of the polygon due to curvature generation and contour stretching (Appendix D). Our main constraint for the time step is

$$dt \leq dt_{\text{dyn}} \equiv \frac{C}{\sqrt{\rho_{\text{max}}}}, \quad C\sqrt{N_{\text{orbits}}} \ll 1, \quad (16)$$

where ρ_{max} is the maximum value of the projected density calculated over all the vertices and N_{orbits} is the number of orbital times. This dynamical criterion can be derived in a simple fashion by studying the particular case of the harmonic oscillator (Appendix D1; see also Alard & Colombi 2005). Since C is inversely proportional to the square root of the number of dynamical times at play, it depends strongly on the type of system studied. Table A1 shows that C ranges from 5×10^{-4} to 0.025 for all the simulations we did. Because of our rather conservative choices for the values of C , the two other constraints on the time step related to polygon refinement, which are derived in Appendix D2, were found in practice to be subdominant compared to equation (16), but it is definitely possible to construct setups where it is not the case.

Diagnostics also consist of performing sanity tests. Energy conservation represents a crucial test. In addition, we also tested conservation of total mass as well as the area of each individual waterbag.⁷

⁶ For the bottom panel, we use $S(\widehat{A\hat{P}B})$ instead of $S(\widehat{APB})$ in equation (12).

⁷ The expressions for total kinetic and potential energy as well as waterbag area are given in Appendix F3.

In the latter case, it is interesting to focus on the worse waterbag at a given time, because this can be used to bound violation to conservation of any casimir.⁸ However, we found in practice that total energy conservation represents the strongest test. As studied in detail in Appendix E, energy conservation remains excellent for all the simulations we did, better than $\sim 2 \times 10^{-4}$ in warm cases and than $\sim 10^{-3}$ in colder configurations, except for one of the randomly perturbed waterbag simulations with unrefinement allowed. As already discussed in Section 2.2.3, unrefinement does indeed introduce long-term noise that worsens energy conservation after a number of dynamical times. With unrefinement inhibited, energy can in fact be conserved at a level better than $\sim 5 \times 10^{-5}$ and $\sim 2 \times 10^{-4}$ in warm and cold cases, respectively.

3 A CONVERGENCE STUDY TO THE COLD CASE: SINGLE WATERBAGS

In this section, we focus on the single-waterbag simulations. The main purpose of this analysis is to study the relaxation of the profile to a quasi-stationary state in the limit when the waterbag becomes infinitely thin, corresponding to the cold case. After a detailed visual inspection of the simulations (Section 3.1), we analyse, in the nearly cold case, the properties of the inner profile that is built during relaxation, starting first with the gravitational potential and its logarithmic slope (Section 3.2), then proceeding with the phase-space energy distribution function (Section 3.3). In a final discussion (Section 3.4), we compare our results to previous works, paying particular attention to measurements in N -body simulations.

3.1 Visual inspection

Figs 6 and 7 display, for each value of the thickness parameter Δp in the range $[0.01, 0.1]$, the phase-space distribution function of the single-waterbag simulations at various times, showing the well-known building up of a quasi-stationary profile with a core and a spiral halo (e.g. Cuperman et al. 1971a,b; Janin 1971). The appearance of the halo arises from the filamentation of the external part of the waterbag, while a compact core survives. Fig. 8 allows one to distinguish the core for the smallest values of Δp . Null for $\Delta p = 1$, where the waterbag keeps a well-defined oscillating balloon shape,⁹ the fraction of the mass feeding the halo increases with $1/\Delta p$, leaving a core of which the projected size varies roughly

⁸ A casimir is given by

$$C[c] \equiv \int c[f(x, v, t)] dx dv = \sum_k c[f_k] V_k, \quad (17)$$

where c is a function assumed here to take finite values at f_k and V_k is the phase-space area of waterbag k . As a consequence of Liouville theorem, casimirs do not depend on time. With $c[f] = f$ and $-f \ln f$, one obtains two notorious casimirs, respectively, the total mass and the Gibbs entropy. The violation on conservation of $c[f]$ can be written as

$$|\Delta C[f]| \leq \max_k |\Delta V_k| \times \sum_l |c[f_l]|, \quad (18)$$

and can thus be bounded in terms of violation to area conservation of the worse waterbag.

⁹ This is due to the fact that initial conditions are very close to a stable single-waterbag stationary solution (see, e.g., Severne & Kuzzell 1975); hence, the waterbag contour oscillates with a small amplitude around this solution.

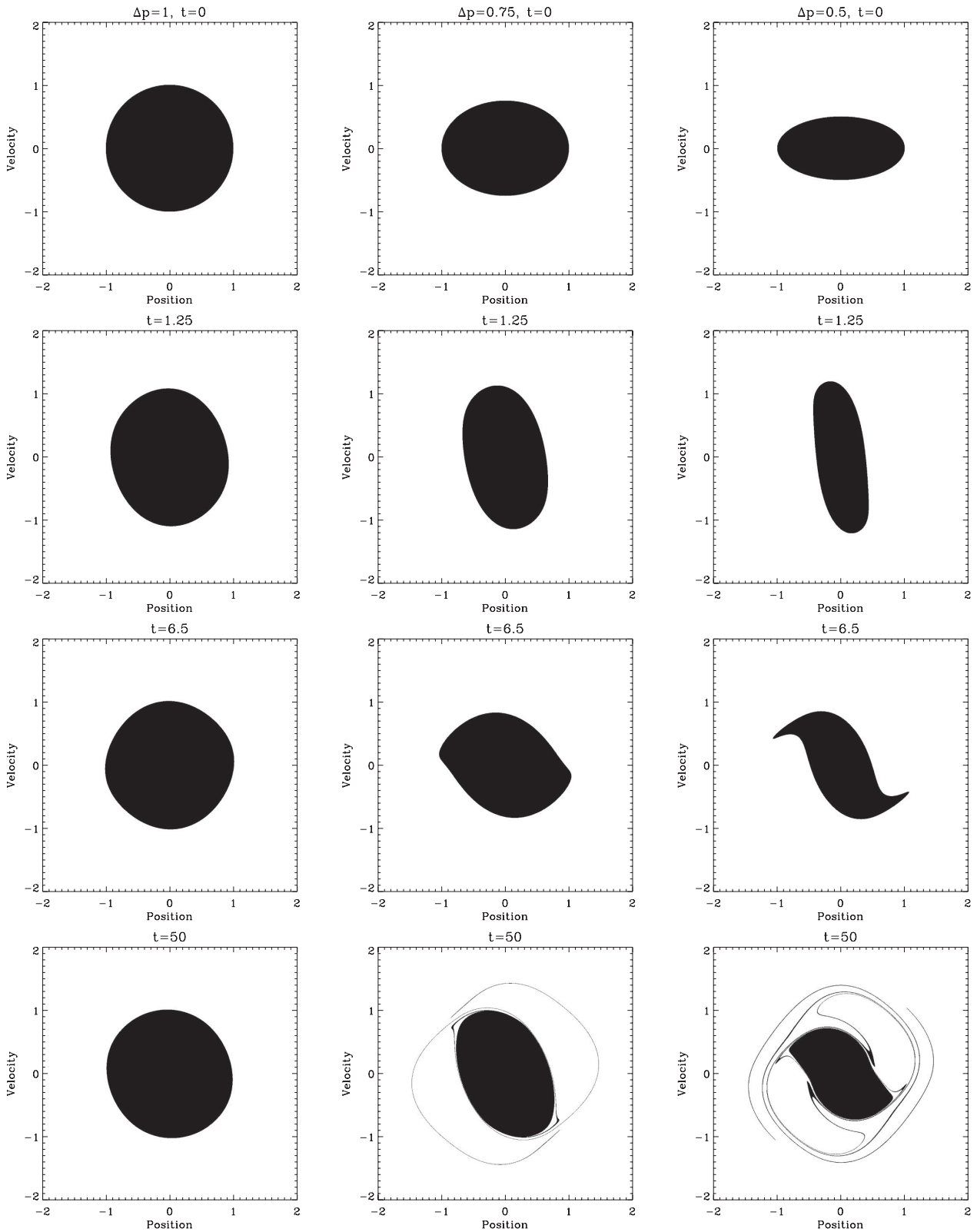


Figure 6. The phase-space distribution function of single-waterbag simulations at various times. Times increases from top to bottom, while the initial velocity dispersion, traced by the parameter Δp , decreases from left to right. The values $t = 1.25$ and 6.5 correspond approximately to collapse time and fourth crossing time, respectively, in the cold case ($\Delta p = 0$).

Downloaded from https://academic.oup.com/mnras/article/44/1/3/2414/1131192 by guest on 24 April 2022

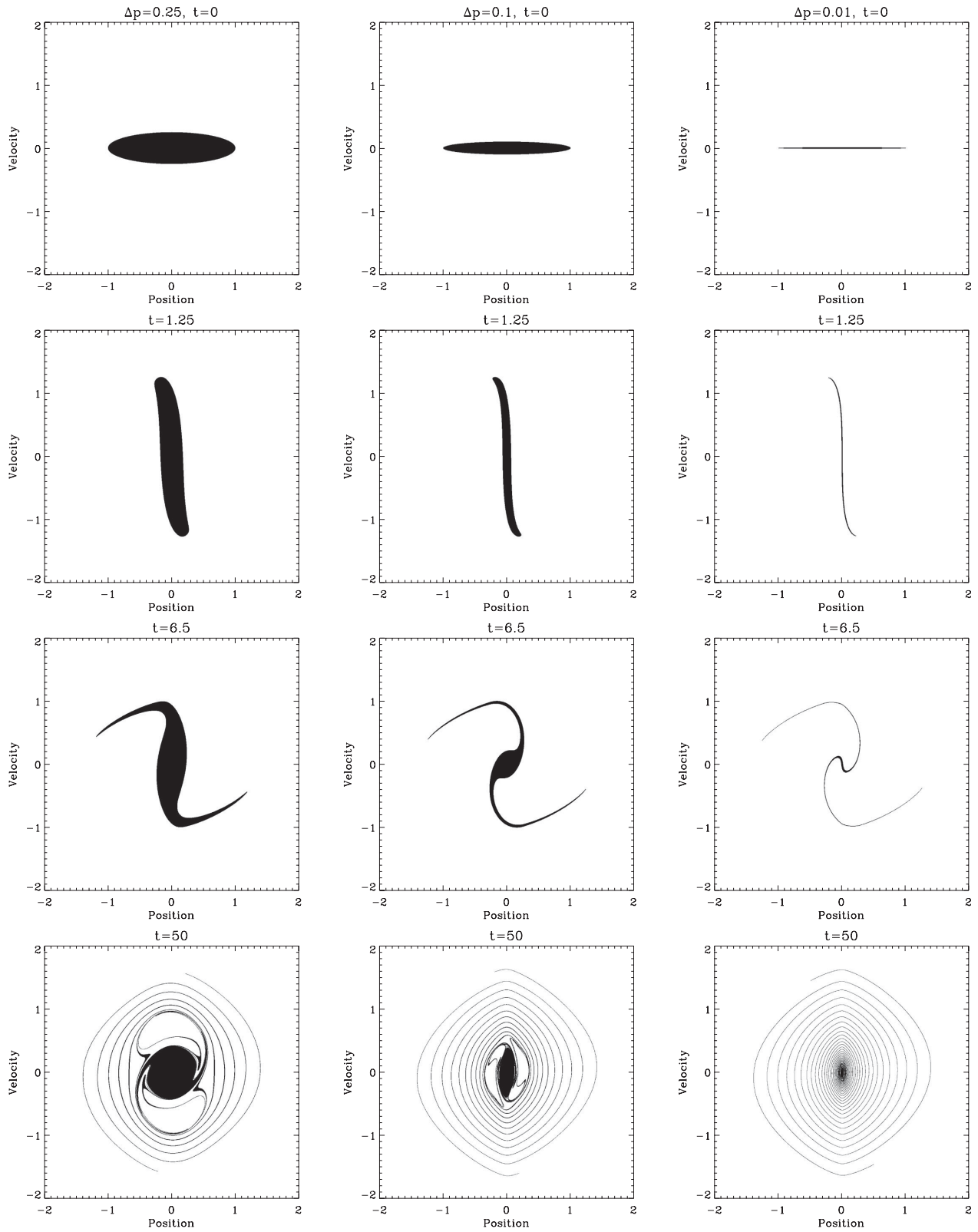


Figure 7. Fig. 6, continued, for smaller values of Δp . For $\Delta p = 0.01$, we show the simulation Tophat0.010 in the nomenclature of Table A1, but the other simulation (Tophat0.010U) would not differ from this one at the level of zoom we are looking at.

Downloaded from https://academic.oup.com/mnras/article/44/1/3/2414/1131192 by guest on 24 April 2022

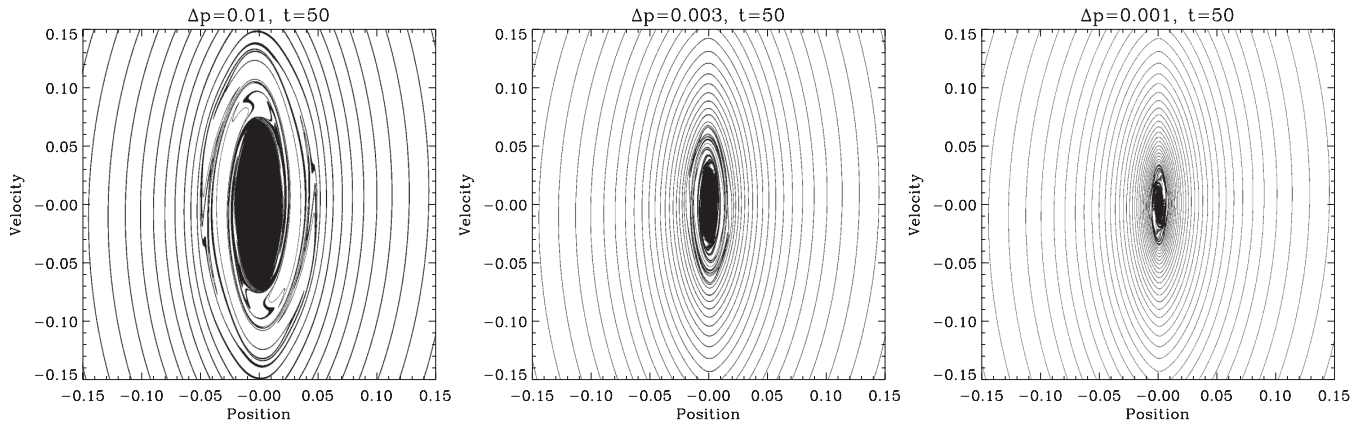


Figure 8. A zoom in phase-space on the central part of the system at final time, for $\Delta p = 0.01$ (left), 0.003 (middle) and 0.001 (right). The simulations adopted here are Tophat0.010, Tophat0.003 and Tophat0.001 in the nomenclature of Table A1. With the same initial conditions but slightly different parameters for performing the simulations (as listed in Table A1), some small differences can be sighted. They simply indicate a shift in effective dynamical time due to a slight change in the energetic state of the system from one simulation to another.

with $\Delta p^{0.8}$ for $\Delta p \lesssim 0.1$.¹⁰ In all the cases except for $\Delta p = 1$, there is a region between the halo and the core where the system presents an unstable behaviour. The extension of this region is of the same order of that of the core. Note also, from inspection of Fig. 8, that the shape of the spiral remains the same whatever $\Delta p \lesssim 0.01$ when far enough from the centre: in agreement with intuition, the details of the shape of the central region in the vicinity of the core do not influence the dynamics of the outer spiral. The shape of this spiral can be computed analytically under the assumption of self-similarity (Alard 2013), which, as discussed in next section, applies at least to some extent to our cold waterbags.

Figs 9 and 10 focus on the perturbed waterbag, with a comparison to its unperturbed counterpart in phase-space and in Action–Angle space, respectively. The presence of random perturbations induces the formation of substructures and also makes the extension of the unstable region in the centre of the system much larger, as illustrated by the four right-hand panels of Fig. 9. Another interesting property is that filaments tend to pack together in phase-space, leaving larger empty regions than in the unperturbed case: this is particularly visible when comparing the two bottom panels of Fig. 10.

Fig. 11 displays the total length of the waterbag as a function of time for small values of Δp .¹¹ Without perturbation, the length behaves soon as a power law of time of index 1.28 for $t \gtrsim 10$, a result which might again be interpreted in terms of a self-similar spiral (Alard 2013). In the perturbed case, the length seems, not surprisingly, to increase faster than a power law although we could perform an indicative fit at late time with a logarithmic slope of 3.2.

3.2 The gravitational potential

The gravitational potential is shown at various times in the $\Delta p = 0.001$ case in the top-left panel of Fig. 12. The initial conditions correspond to an approximately harmonic potential with $\phi(x) - \phi_{\min} \propto x^2$ (green line). As discussed further in Section 3.3, in the pure cold case, the projected density presents a singularity in the centre such that $\phi(x) - \phi_{\min} \propto x^{4/3}$ at collapse time and subse-

quent crossing times. This is indeed the case for our measurements if one stays sufficiently far away from the centre (blue line, which superposes well the dotted curve). However, the system relaxes very rapidly to a quasi-stationary state. The overall profile of the latter follows rather well a power law of the form $\phi(x) - \phi_{\min} \propto x^{3/2}$ (Binney 2004, red dots). There are some noticeable deviations from such a power law, which we discuss now.

To examine more in detail the scaling behaviour of the potential, one can study its logarithmic slope, which can be defined as

$$\beta(x) = \frac{|a(x)|}{\phi - \phi_{\min}}, \quad (19)$$

where ϕ_{\min} is the minimum of the potential. Because it depends on the acceleration and on the potential, the quantity $\beta(x)$ is a well-behaved estimator. It is expected to be a smooth function of x as shown in top-right panel of Fig. 12 for $\Delta p \leq 0.1$. In our waterbag case, it should tend to 2 in the limit $\phi \rightarrow \phi_{\min}$ as a test of robustness, which is indeed the case. Finally, it is rather insensitive to the presence of the core in the region where this latter should not contribute, as the superposition of the curves in top-right panel of Fig. 12 demonstrate.

Using several simulations with different values of Δp allows us to perform a convergence study to the cold case and in particular to figure accurately where the measurements are influenced by the core. For instance, for $\Delta p = 0.001$, it is reasonable to state that the presence of a core does not affect the measured slope when $x \gtrsim 0.01$, $\phi \gtrsim 10^{-3}$, for which we find $\beta \simeq 1.57$. With the available dynamic range at our disposal, there is no clear convergence of function $\beta(x)$ to a constant at small x . The parameter β seems indeed to continue slowly increasing in magnitude while reaching the smallest scales. The lack of a well-defined power law for the gravitational potential reminds us of the results obtained in the three-dimensional case, where the density profiles of dark matter haloes are found in the most accurate N -body simulations to follow an Einasto profile (see, e.g., Merritt et al. 2006; Navarro et al. 2010). We can only set a firm lower bound for β for small values of x as

$$\beta(x) > 1.54, \quad x \ll 1, \quad (20)$$

by using the lowest possible value of $x \simeq 0.02$ for which the solid and the dotted curves still coincide in upper-right panel of Fig. 12.

In the randomly perturbed simulations, the results, shown in the two bottom panels of Fig. 12 for two different times, are analogous to the unperturbed case, except that they are much more noisy and

¹⁰ Such a power-law behaviour can be derived from the visual examination of top-right panel of Fig. 12.

¹¹ As a complement, bottom panel of Fig. ?? gives the total number of vertices as a function of time for the all single-waterbag simulations we did.

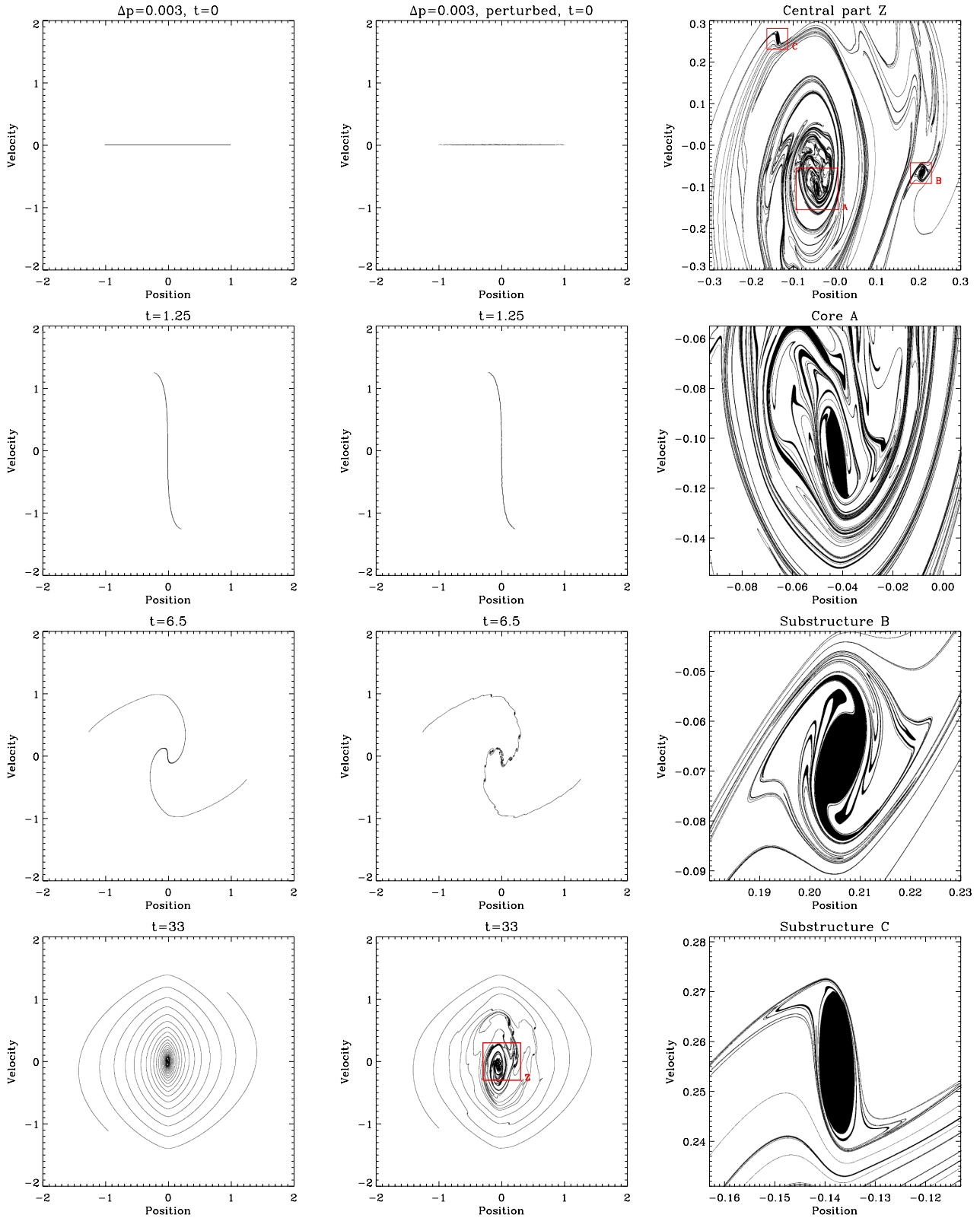


Figure 9. The effect of random perturbations. The left-hand column of panels shows, similarly as in Figs 6 and 7, the evolution of a waterbag with $\Delta p = 0.003$. The middle column is alike, but when random perturbations have been added on to the waterbag. The four right-hand panels correspond to successive zooms on the central part of the system (top panel), the core (second panel) and two ‘subhaloes’ (bottom panels). If initial conditions would be actually cold, it is reasonable to postulate that the substructures would present an exactly similar shape in phase-space to the unperturbed case. The simulations used here are Tophat0.003 and Perturbed in the nomenclature of Table A1. Note as discussed in the previous figure captions, other simulations would give a very similar result, except for a very slight dynamical shift.

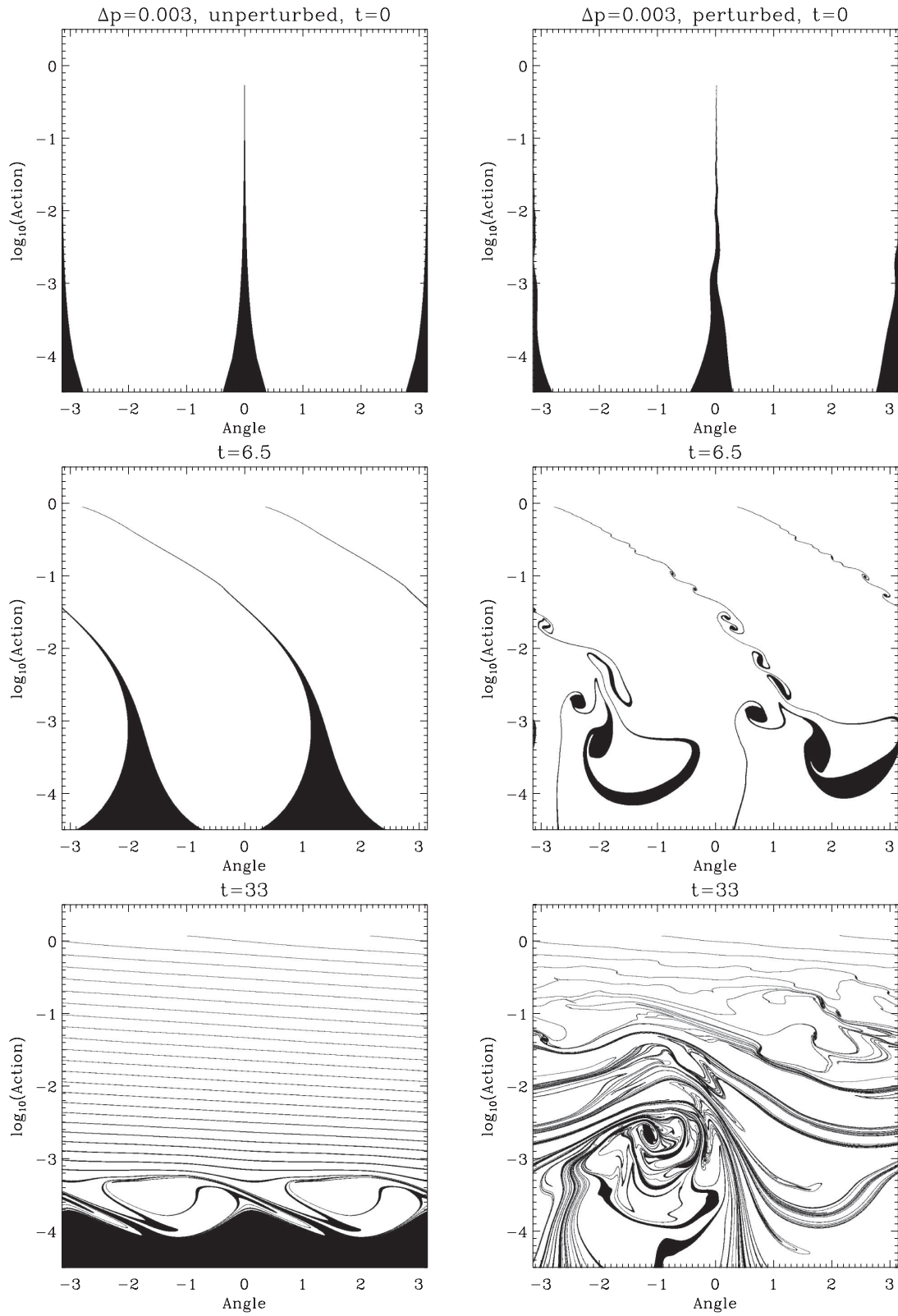


Figure 10. Representation in Action–Angle space of the simulations of Fig. 9. On the left, the unperturbed single-waterbag simulation with $\Delta p = 0.003$ and on the right, the randomly perturbed waterbag.

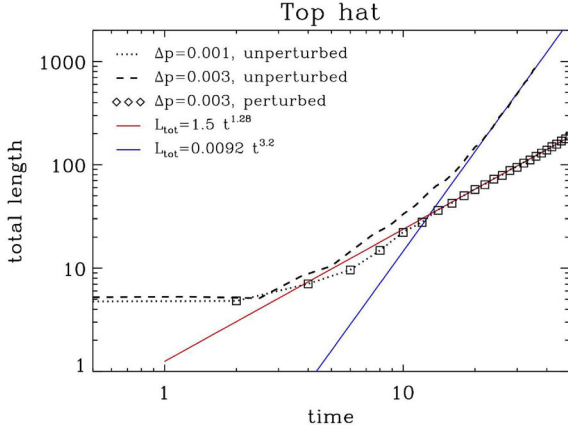


Figure 11. The total length of the waterbag contour as a function of time. We consider here our coldest setups, with $\Delta p = 0.001$ and 0.003 , as well as the randomly perturbed $\Delta p = 0.003$ waterbag. In the unperturbed case, the total length soon behaves roughly like a power law as indicated by the red line. Random perturbations induce the appearance of numerous substructures and increased filamentation: the length soon augments much faster with time than for the unperturbed case. The blue line shows a late-time power-law fit, but this is obviously only indicative, as it seems clear that the length increases with time faster than a power law. The measurements have been made for the simulations Tophat0.001, Tophat0.003 and Perturbed in the nomenclature of Table A1, but would not change for other runs we performed with the same initial conditions.

that the system builds a much larger ‘core’ than in the unperturbed simulations. We use quotes, because this region of approximate constant projected density is in fact quite intricate in phase-space and rather ‘chaotic’. Its projected size seems to range between those of the $\Delta p = 0.01$ and 0.1 unperturbed simulations. Our measurements in the perturbed case are however inconclusive, because we were unable to follow the system during sufficiently many dynamical times to have reached an actually quasi-steady-state and we tested only one specific kind of perturbations. So from now on, unless specified otherwise, we discuss the unperturbed case corresponding to the top panels of Fig. 12.

3.3 The phase-space energy distribution function

To understand more deeply the establishment of a steady state after relaxation, it is useful to study the phase-space energy distribution function, $f_E(E)$, as

$$f_E(E) \equiv \lim_{\delta E \rightarrow 0} \frac{\int_{E(x,v) \in [E, E+\delta E]} f(x,v) dx dv}{\int_{E(x,v) \in [E, E+\delta E]} dx dv}, \quad (21)$$

which provides the average of the phase-space density per energy level. For systems where the phase-space density depends only on energy, the equality $f(x,v) = f_E[E(x,v)]$ stands. The way we compute function $f_E(E)$ is detailed in Appendix H.

Fig. 13 displays the phase-space distribution function measured in our thinnest waterbags. The upper-left panel shows function $f_E(E)$ at various times. Except for $t = 0$ and 50 , which correspond, respectively, to initial conditions and final time, the other snapshots considered have been chosen carefully to coincide with crossing times, that is, to moments when the central part of the curve supporting $f(x,v,t)$ is vertical in phase-space, such as in the two middle panels of the left-hand column of Fig. 9. The first striking result is that function $f(E)$ presents a remarkable power-law behaviour at small energies, which is already present at collapse time ($t = 1.25$)!

Furthermore, convergence to a steady state is very fast: at the second crossing time ($t = 3.6$), the energy distribution at small E is already converged. The third crossing is enough to get nearly the correct shape for the full final energy spectrum.

At this point, since collapse time seems to provide an interesting power-law slope for the energy, we might try to compute it analytically. Given the properties of the initial projected density profile,

$$\rho_0(x) \equiv \rho(x, t = 0) = \frac{2}{\pi} \sqrt{1 - x^2}, \quad (22)$$

$$\simeq \bar{\rho}_0 (1 - 3ax^2), \quad x \ll 1, \quad (23)$$

with $\bar{\rho}_0 = 2/\pi$ and $a = 1/6$, we can easily calculate the phase-space energy distribution function in the small energy limit to understand both the power-law behaviours observed in upper-left panel of Fig. 13 at $t = 0$ and at collapse time, $t \equiv t_c$. Details of this calculation are provided in Appendix J.

Initial conditions correspond to an approximately harmonic potential

$$\phi - \phi_{\min} \simeq \frac{1}{2} \bar{\rho}_0 x^2, \quad x \ll 1 \quad (24)$$

(green line in upper-left panel of Fig. 12), and

$$f_E(E, t = 0) = \frac{\sqrt{\bar{\rho}_0 a}}{\sqrt{2\pi}} \left[\frac{a(E - E_{\min})}{\bar{\rho}_0} \right]^{-1/2}, \quad (25)$$

$$\simeq 0.143(E - E_{\min})^{-1/2}, \quad (26)$$

for $E - E_{\min} \ll 1$, where $E_{\min} = \phi_{\min}$ is the minimum of energy. This result agrees perfectly with our measurements, as shown by the orange dashed line in upper-left panel of Fig. 13.

At collapse time, the projected density becomes singular, $\rho(x) \propto x^{-2/3}$, corresponding to a potential of the form

$$\phi - \phi_{\min} \simeq \frac{3}{2} \frac{\bar{\rho}_0}{a} (\sqrt{ax})^{4/3}, \quad x \ll 1 \quad (27)$$

(blue line in upper-left panel of Fig. 12), and

$$f_E(E, t_c) = \frac{(3/2)^{3/4} \Gamma(5/4) \sqrt{\bar{\rho}_0 a}}{4\sqrt{\pi} \Gamma(7/4)} \left[\frac{a(E - E_{\min})}{\bar{\rho}_0} \right]^{-3/4}, \quad (28)$$

$$\simeq 0.168(E - E_{\min})^{-3/4}, \quad (29)$$

in the limit $E - E_{\min} \ll 1$, again in very good agreement with our measurements as shown by the grey line in upper-left panel of Fig. 13. Note that the power-law index of $-3/4$ in equation (28) should be obtained for small values of $E - E_{\min}$ at each crossing time.

Now, suppose that mixing happens in such a way that the system relaxes to a stationary state preserving the phase-space energy distribution function obtained at crossing time:

$$f(x,v) = f_E[E(x,v)] = A [E(x,v) - E_{\min}]^{-\gamma}. \quad (30)$$

This implies, by solving Poisson equation,

$$\phi = E_{\min} + \phi_0 x^\beta \quad (31)$$

with

$$\beta = \frac{4}{1 + 2\gamma}, \quad (32)$$

$$\phi_0 = \left(\frac{\pi}{2} \right)^{-\frac{1}{1+2\gamma}} \left[\frac{A(1 + 2\gamma)^2 \Gamma(-1/2 + \gamma)}{(3 - 2\gamma)\Gamma(\gamma)} \right]^{\frac{2}{1+2\gamma}}. \quad (33)$$

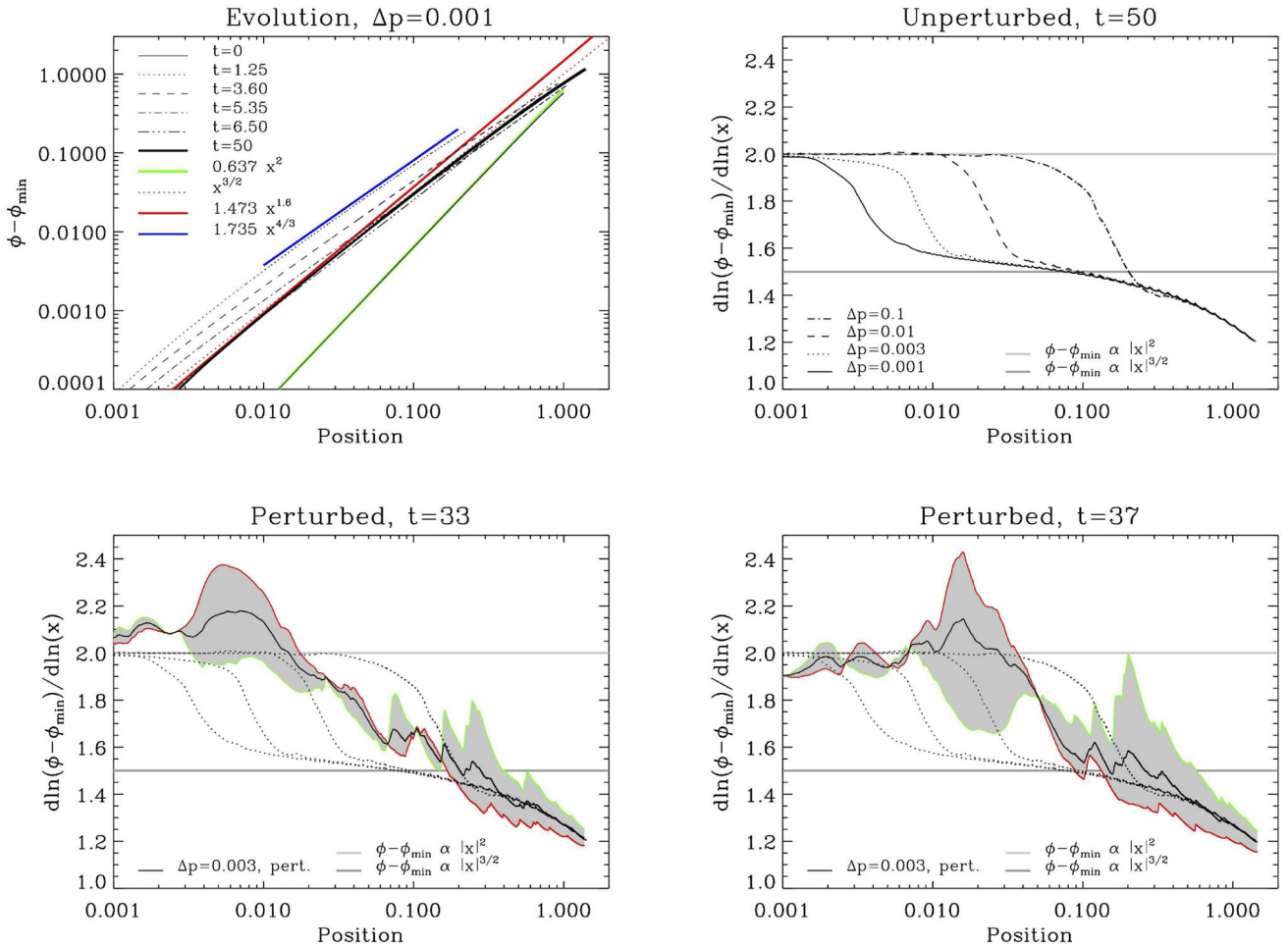


Figure 12. The gravitational potential properties in the cold case. In the top-left panel, the potential is plotted for the $\Delta p = 0.001$ case as a function of scale at various times, starting from initial conditions. Except for the last snapshot of the simulation, $t = 50$, the curves with $t > 0$ correspond to the first four crossing times. The green and the blue line stand for analytic predictions of Section 3.3, respectively, for initial conditions and collapse time. The red power law is the result of assuming an average phase-space density per energy level proportional to that obtained at collapse time, as discussed in Section 3.3, while the dotted one corresponds to a conjecture of Binney (2004) based on measurement on N -body simulations. The top-right panel displays the logarithmic slope of the gravitational potential, for various values of Δp in order to be able to perform a convergence study. The bottom and top grey lines correspond, respectively, to the index predicted by Binney and the one expected when a core dominates at the centre. The two bottom panels show the logarithmic slope measured in the perturbed case, at two different times. There is a grey shaded area bordered by a green and a red contour. These two contours correspond to the measurement of the potential on each side of its minimum, while the black curve is the average between them. In addition, the measurements displayed in top-right panel are shown as dotted curves. This figure uses simulations Tophat0.001, Tophat0.003, Tophat0.010, Tophat0.100 and Perturbed in the nomenclature of Table A1, but it would not change significantly for other runs we performed with the same initial conditions.

Fitting the form (30) with the power-law index $\gamma = 3/4$ on the low-energy part of the final stage of our thin waterbag simulations (top-right panel of Fig. 13) gives $A = 0.105$ and indeed agrees to a great accuracy with the measured function $f_E(E)$ at small energies over about a decade. This in turns implies

$$\beta = 8/5 = 1.6, \quad (34)$$

and $\phi_0 = 1.473$, in excellent agreement with our measurements of the potential at small scales, as indicated by the red line in top-left panel of Fig. 12 and consistent with the direct measurements of the logarithmic slope of the potential performed in Section 3.2, which indicated $\beta(x) > 1.54$ for $x \ll 1$. This result is clearly non-trivial when examining right-hand panel of Fig. 8 in regions of interest not contaminated by the core, e.g. $0.01 \lesssim r \lesssim 0.05$, where mixing is very strong in the form of a dense spiral structure. Note however that even though the value $\beta = 8/5$ represents a good candidate for the asymptotic logarithmic slope of the gravitational potential

at small scales, our measurements do not present yet the required dynamic range to provide a firm numerical proof of this.

To complete this analysis, bottom-right panel of Fig. 13 shows the phase-space energy distribution function for the randomly perturbed waterbag with $\Delta p = 0.003$. Modulo the large amount of fluctuations induced by substructures, it is interesting to note that the energy spectrum agrees with that of the unperturbed case. However, as mentioned in Section 3.2, we did not follow this randomly perturbed system for sufficiently long time to make any definitive conclusions.

3.4 Discussion

Our measurements of the logarithmic slope $\beta(x)$ of the gravitational potential suggest a slowly running power-law index with $\beta(x) > 1.54$ in the limit $x \ll 1$. They are consistent with a theoretical asymptotic value $\beta = 1.6$ computed by assuming that the average phase-space density per energy level remains conserved between

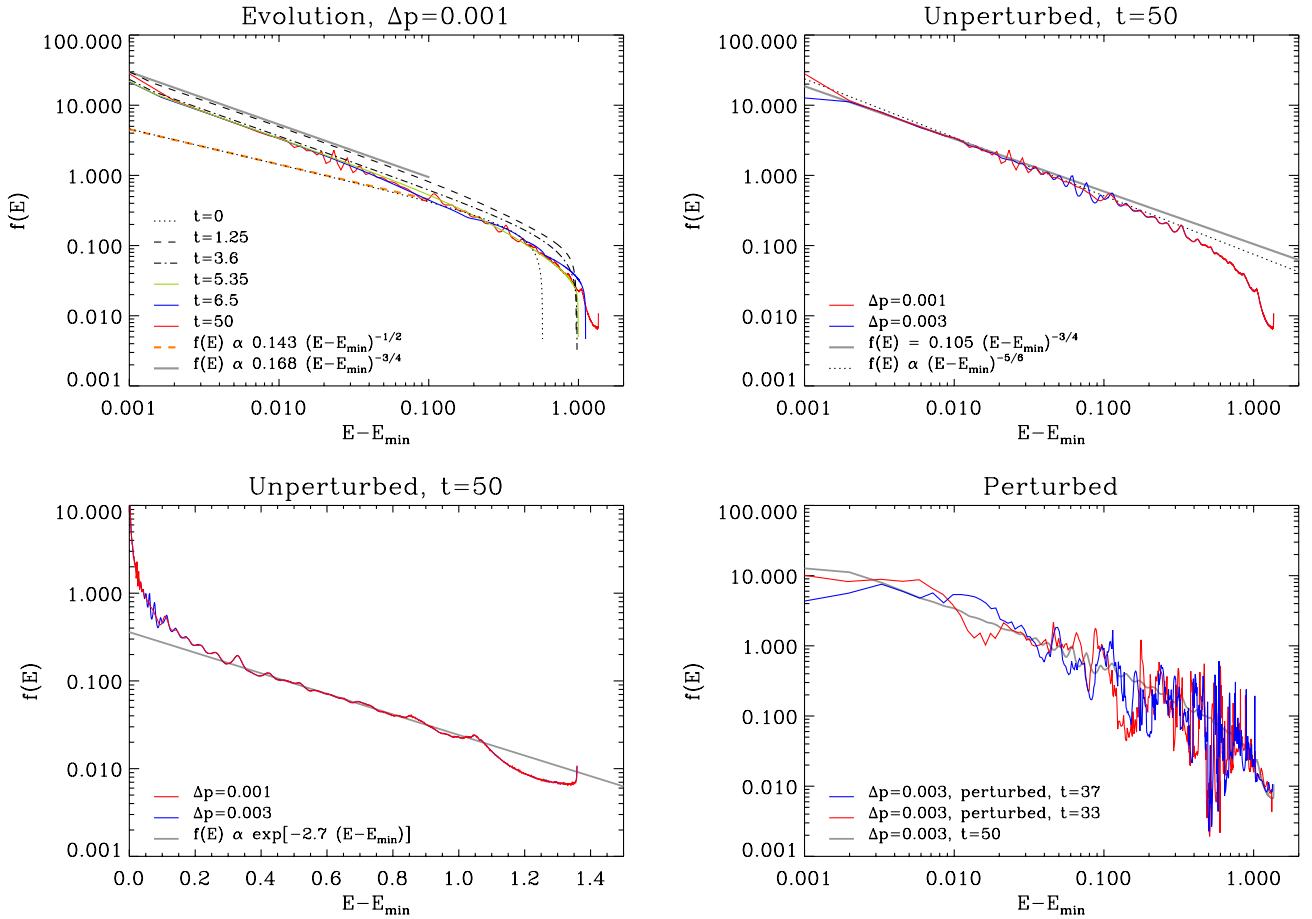


Figure 13. The phase-space energy distribution function in our close-to-cold waterbag simulations with $\Delta p = 0.001$ and 0.003 . In the upper-left panel, the function $f_E(E)$ is shown for $\Delta p = 0.001$ at various times, corresponding to initial conditions, first to fourth crossing times and final time. The dashed orange and the solid grey line correspond to analytic predictions (25) and (28). In the upper-right panel, the function $f_E(E)$ is shown at last time, $t = 50$, for $\Delta p = 0.001$ and 0.003 and fitted with power laws of index $-3/4$ and $-5/6$, the latter value corresponding to the conjecture of Binney (2004). The bottom-left panel is analogous to the upper-right one, but a linear scale has been chosen for $E - E_{\min}$ to emphasize the exponential behaviour of function $f_E(E)$ at largest energies. The bottom-right panel compares measurements of $f_E(E)$ in the randomly perturbed $\Delta p = 0.003$ at two different times to the unperturbed case. The measurements are shown for the simulations Tophat0.001, Tophat0.003 and Perturbed in the nomenclature of Table A1, but would not change significantly for other runs we performed with the same initial conditions. Note also, as explained in Appendix H, that the measurements are performed in 1023 bins spaced linearly between the minimum and maximum of the energy. This means that function $f_E(E)$ plotted in each panel represents a smoothed version of the actual energy spectrum which has much more structure. Note also that the first bin, corresponding to $E - E_{\min} \sim 10^{-3}$ is expected to be spurious, because it corresponds to the smallest energy bin, which does not have a ring shape in phase-space, but is homeomorphic to a disc. The measurements should thus be examined for $E \gtrsim 2 \times 10^{-3}$, which correspond to energy shells in phase-space that are not affected by the central core in the unperturbed cases.

crossing times. They thus disagree unarguably with the conjecture $\beta = 1.5$ of Binney (2004) as well as with the value $\beta = 10/7 \simeq 1.43$ obtained by Gurevich & Zybin (1995) by assuming adiabatic invariance from collapse time. Although we do not have sufficient dynamical range to make strong claims, this result also seems to contradict the measurements of Schulz et al. (2013) in N -body simulations, who find a well-defined power-law behaviour of the projected density profile at small x corresponding to $\beta \simeq 1.53$. Measuring $\rho(x)$ is a difficult task for us, because of the near-caustic structures that the projected density is subjected to. Schulz et al. (2013) also used the interior mass profile, that is, the acceleration modulus $|a(x)|$ to measure the slope, but they argue that this integral quantity is contaminated by the core up to rather large values of x . Note that their measurements using this estimator give slightly larger values of β , so are more consistent with ours. They also propose a Lagrangian estimator using the Action Ω as a function of enclosed mass inside the surface inside contours of constant energy. This estimator, as constructed by the authors, can be used

as long as Ω remains a monotonic function of particle rank. With this estimator, they find $\beta \simeq 1.59$, in very good agreement with our theoretical predictions and consistent with our measurements! They however argue that measurements of β based on this estimator are not determinant because they can be performed only at early times of the simulations: they prefer at the end to emphasize on the value of β obtained from $\rho(x)$, which is measured at late times. We believe that the logarithmic slope of the gravitational potential, equation (19), remains a robust estimator, even if applied to an N -body simulation. It would be interesting to use such an estimator in the N -body simulations of Schulz et al. (2013) to see if it leads to the same conclusions as their density-based estimator or if it would agree better, in fact, with their Action-based estimator.

Besides the fact that we are using a different estimator for measuring the inner slope of the profile, another plausible explanation of our disagreement with Schulz et al. (2013) is that the noise introduced by their particle-based approach might lead, after sufficient time, to the wrong numerical attractor. A clue to this is that they

found some gaps in phase-space in their simulations, which might be the signature of a resonant instability induced by the discreteness of the representation, similarly as what we found in the Gaussian simulation of Fig. 2 when only a few waterbags were used to represent the phase-space distribution function. Our single-waterbag simulations present such features, but only in the very vicinity of the core and with negligible consequence on the measurement of the inner slope if a proper estimate of the trustable scaling range is performed.

4 CONCLUSION

In this paper, we have revisited with a modern perspective the so-called waterbag method to solve numerically Vlasov–Poisson equations in one-dimensional gravity, recasting in detail and testing thoroughly the method we introduced briefly in Colombi & Touma (2008). We have shown how to represent the phase-space distribution function with a set of waterbags sampled with an orientated polygon, to compute in a self-consistent way its dynamical evolution and to analyse its properties with the appropriate treatment of the polygonal structure.

The method is entropy conserving so it allows one to follow extremely accurately the evolution of a system, even in the presence of highly non-linear instabilities. But because it aims at preserving all the details that appear in phase-space during the course of the dynamics, the method is very costly: when there is mixing, the computational cost increases at least linearly with the number of dynamical times and becomes exponential when the system is chaotic. Our calculations were however limited by the fact that our code is serial. Parallelization of the code and running it on supercomputers might alleviate partly these limitations.

To preserve the increasing complexity of the waterbag contours, we proposed a sophisticated and robust refinement scheme to add vertices to the orientated polygon using a geometric construct interpolating local curvature, while our main refinement criterion was based on phase-space area conservation. In two-dimensional phase-space, this is exactly equivalent to enforcing conservation of the following Poincaré invariant, which can be defined in $2N$ -dimensional phase-space as

$$I \equiv \oint \mathbf{v} \cdot d\mathbf{x}(s), \quad (35)$$

where the contour integral is performed on a closed curve in phase-space composed of points following the equations of motion. This Poincaré invariant thus provides a natural tool to extend our refinement criterion to higher number of dimensions.

Unrefinement, which consists of removing vertices from the polygon when they are not needed anymore, is potentially powerful, because it can decrease the computational cost of the simulation while preserving the same level of accuracy. However, we showed that successive refinement/unrefinements of a waterbag contour element are unavoidable and introduce a long-term noise contribution that can worsen significantly energy conservation when following a system during many dynamical times. However, all our simulations with unrefinement were still very accurate, except for one. Unrefinement might become a must in higher number of dimensions, due to the considerably larger contrasts in the various dynamical states a contour element can go through. This will be examined in a separate work on systems with spherical symmetry, which present one more dimension of angular momentum in phase-space but can also be approached with the waterbag method (Colombi & Touma 2008).

In six-dimensional phase-space, the waterbag method is very challenging to implement in the warm case due to its extreme cost in memory and computational time: indeed the waterbag contours correspond to five-dimensional hypersurfaces. Cold initial conditions, which are relevant in cosmology, seem on the other hand approachable. In this case, the phase-space distribution is supported by a three-dimensional sheet evolving in six-dimensional phase-space. An additional difficulty arises, however, from the fact that it is needed to soften the gravitational force to avoid numerical instabilities induced by the presence of singularities. A question then is how well the true gravitational dynamics is described by its softened counterpart.¹² In current proposed implementation, which does not yet include local refinement of the phase-space sheet (Hahn et al. 2013), the three-dimensional phase-space sheet is sampled with simplices (Abel, Hahn & Kaehler 2012; Shandarin, Habib & Heitmann 2012). The method is thus analogous to the waterbag method in the sense that it preserves connectivity. Again, in presence of very needed refinement, the computational cost of such simulations will increase very quickly with the number of dynamical times at play: it seems important to investigate optimal refinement algorithms, which might include unrefinement as discussed above and should take into account of the anisotropic nature of the dynamics.

Behaviour of gravitational systems at large times in the continuous limit is still badly understood except in some very particular cases (see, e.g., Mouhot & Villani 2011). Even in the one-dimensional gravitational case studied in this paper, the long-term properties of systems as functions of initial conditions remain an open debate, because it is very challenging to follow them numerically. Particle-based methods can rapidly introduce resonant instabilities that drive the system to attractors far from the exact solution. The cold case, where the initial projected density is locally of the form (23), represents a good example of this state of facts. In this paper, by studying a set of single-waterbag simulations with decreasing thickness, we performed a convergence study to the cold case and analysed in detail the inner structure of the steady state that builds up during relaxation. We measured the properties of the gravitational potential and the energy spectrum of the system. We found that the gravitational potential profile after relaxation is consistent with a running power law as

$$\phi(x) \propto x^{\beta(x)}, \quad (36)$$

where $\beta(x)$ is a slowly decreasing function of x , roughly averaging to $\beta \simeq 3/2$ in agreement with the conjecture of Binney (2004). Close to the centre, we found

$$\beta > 1.54 \quad (37)$$

in disagreement with recent results of the literature based on N -body experiments (Binney 2004; Alard 2013; Schulz et al. 2013). In fact, our measurement are consistent with

$$\beta = 8/5 = 1.6 \quad (38)$$

at the centre of the system, a value which can be predicted explicitly by assuming that the average phase-space density per energy level is conserved between crossing times.

Our simulations do not present sufficient dynamical range to demonstrate numerically that $\beta = 8/5$ corresponds to the expected

¹² This is the reason why, in this work, we studied convergence to the cold case with very cold but not infinitely thin waterbags.

asymptotic singular behaviour of the gravitational potential profile of cold systems in one dimension, but the disagreement of our measurements with the thorough N -body experiments of Schulz et al. (2013) is puzzling. These results are very worrying for the N -body approach. Indeed, in three dimensions, many important results on the structures of dark matter haloes are based on measurements in N -body simulations (see, e.g., Navarro, Frenk & White 1996, 1997; Navarro et al. 2010; Diemand & Moore 2011, and references therein). This definitely justifies the need for developing alternative methods to solve Vlasov–Poisson without resorting to particles.

ACKNOWLEDGEMENTS

We thank Tom Abel, Christophe Alard, James Binney, Walter Dehnen, Christophe Pichon and Scott Tremaine for useful discussions. The analytic calculations of Section 3.3 and Appendix J have been performed with MATHEMATICA. JT acknowledges the support of an Arab Fund Fellowship for the year 2013–2014. This work has been funded in part by ANR grant ANR-13-MONO-0003-01 as well as NSF grants AST-0507401 and AST-0206038.

REFERENCES

Abel T., Hahn O., Kaehler R., 2012, *MNRAS*, 427, 61
 Alard C., 2013, *MNRAS*, 428, 340
 Alard C., Colombi S., 2005, *MNRAS*, 359, 123
 Bertschinger E., 1985, *ApJS*, 58, 39
 Bertschinger E., 1998, *ARA&A*, 36, 599
 Besse N., Latu G., Ghizzo A., Sonnendrücker E., Bertrand P., 2008, *J. Comput. Phys.*, 227, 7889
 Binney J., 2004, *MNRAS*, 350, 939
 Camm G. L., 1950, *MNRAS*, 110, 305
 Campa A., Dauxois T., Ruffo S., 2009, *Phys. Rep.*, 480, 57
 Campos Pinto M., 2007, *Int. J. Appl. Math. Comput. Sci.*, 17, 351
 Campos Pinto M., 2011, preprint (arXiv:1112.1859)
 Carron J., Szapudi I., 2013, *MNRAS*, 432, 3161
 Chavanis P.-H., 2006, *Physica A*, 365, 102
 Cheng C. Z., Knorr G., 1976, *J. Comput. Phys.*, 22, 330
 Colombi S., 2001, *New Astron. Rev.*, 45, 373
 Colombi S., Touma J., 2008, *Commun. Nonlinear Sci. Numer. Simul.*, 13, 46
 Crouseilles N., Respaud T., Sonnendrücker E., 2009, *Comput. Phys. Commun.*, 180, 1730
 Crouseilles N., Mehrenberger M., Sonnendrücker E., 2010, *J. Comput. Phys.*, 229, 1927
 Cuperman S., Harten A., Lecar M., 1971a, *Ap&SS*, 13, 411
 Cuperman S., Harten A., Lecar M., 1971b, *Ap&SS*, 13, 425
 Dehnen W., Read J. I., 2011, *Eur. Phys. J. Plus*, 126, 55
 DePackh D. C., 1962, *J. Electr. Contrib.*, 13, 417
 Diemand J., Moore B., 2011, *Adv. Sci. Lett.*, 4, 297
 Dolag K., Borgani S., Schindler S., Diaferio A., Bykov A. M., 2008, *Space Sci. Rev.*, 134, 229
 Filbet F., Sonnendrücker E., Bertrand P., 2001, *J. Comput. Phys.*, 172, 166
 Fillmore J. A., Goldreich P., 1984, *ApJ*, 281, 1
 Fujiwara T., 1981, *PASJ*, 33, 531
 Fujiwara T., 1983, *PASJ*, 35, 547
 Gurevich A. V., Zybin K. P., 1995, *Phys.-Usp.*, 38, 687
 Hahn O., Abel T., Kaehler R., 2013, *MNRAS*, 434, 1171
 Hénon M., 1964, *Ann. Astrophys.*, 27, 83
 Hjorth J., Williams L. L. R., 2010, *ApJ*, 722, 851
 Hockney R. W., Eastwood J. W., 1988, *Computer Simulation Using Particles* BristolAdam Hilger
 Janin G., 1971, *A&A*, 11, 188
 Joyce M., Worrakitpoonpon T., 2010, *J. Stat. Mech.: Theor. Exp.*, 10, 12
 Joyce M., Worrakitpoonpon T., 2011, *Phys. Rev. E*, 84, 011139

Lorensen W. E., Cline H. E., 1987, *Comput. Graph.*, 21, 163
 Lynden-Bell D., 1967, *MNRAS*, 136, 101
 Lynden-Bell D., Wood R., 1968, *MNRAS*, 138, 495
 Mehrenberger M., Violard E., Hoenen O., Campos Pinto M., Sonnendrücker E., 2006, *Nucl. Instrum. Methods Phys. Res. A*, 558, 188
 Melott A. L., 2007, preprint (arXiv:0709.0745)
 Melott A. L., Shandarin S. F., Splinter R. J., Suto Y., 1997, *ApJ*, 479, L79
 Merritt D., Graham A. W., Moore B., Diemand J., Terzić B., 2006, *AJ*, 132, 2685
 Mouhot C., Villani C. W. E., 2011, *Acta Math.*, 207, 29
 Navarro J. F., Frenk C. S., White S. D. M., 1996, *ApJ*, 462, 563
 Navarro J. F., Frenk C. S., White S. D. M., 1997, *ApJ*, 490, 493
 Navarro J. F. et al., 2010, *MNRAS*, 402, 21
 Nishida M. T., Yoshizawa M., Watanabe Y., Inagaki S., Kato S., 1981, *PASJ*, 33, 567
 Pontzen A., Governato F., 2013, *MNRAS*, 430, 121
 Roberts K. V., Berk H. L., 1967, *Phys. Rev. Lett.*, 19, 297
 Rybicki G. B., 1971, *Ap&SS*, 14, 15
 Schulz A. E., Dehnen W., Jungman G., Tremaine S., 2013, *MNRAS*, 431, 49
 Severne G., Kuzzell A., 1975, *Ap&SS*, 32, 447
 Shandarin S., Habib S., Heitmann K., 2012, *Phys. Rev. D*, 85, 083005
 Shoucri M. M., Gagne R. R. J., 1978, *J. Comput. Phys.*, 27, 315
 Sonnendrücker E., Roche J., Bertrand P., Ghizzo A., 1999, *J. Comput. Phys.*, 149, 201
 Spitzer L., Jr, 1942, *ApJ*, 95, 329
 Umeda T., 2008, *Earth Planets Space*, 60, 773
 Watanabe Y., Inagaki S., Nishida M. T., Tanaka Y. D., Kato S., 1981, *PASJ*, 33, 541
 Yamaguchi Y. Y., 2008, *Phys. Rev. E*, 78, 041114
 Yamashiro T., Gouda N., Sakagami M., 1992, *Proc. Theor. Phys.*, 88, 269
 Yoshikawa K., Yoshida N., Umemura M., 2013, *ApJ*, 762, 116

APPENDIX A: INITIAL CONDITIONS AND SIMULATION SETTINGS

In this appendix, we provide a full description of the initial conditions of the simulations performed in this work, while Table A1 gives all the simulation settings.

(i) The Gaussian initial conditions are created as follows. Setting

$$G(x, v) \equiv \rho_G \exp\left(-\frac{1}{2} \frac{x^2 + v^2}{\sigma_G^2}\right), \tag{A1}$$

we write

$$f(x, v) = G(x, v), \quad x^2 + v^2 \leq \mathcal{R}^2, \tag{A2}$$

$$= G(x, v) \times \max\left[1 + 2 \operatorname{th}\left(\frac{\mathcal{R} - \sqrt{x^2 + v^2}}{\eta_G}\right), 0\right], \quad x^2 + v^2 > \mathcal{R}^2. \tag{A3}$$

Our initial distribution function is thus a truncated Gaussian. The practical choice of the parameters corresponds to $\mathcal{R} = 1$, $\rho_G = 4$, $\sigma_G = 0.2$ and $\eta_G = 0.02$, which makes the total mass of the system approximately equal to unity for a Gaussian truncated at 5σ .

(ii) The ensemble of stationary clouds initial conditions are created as follows. Each of these haloes initially approximates the stationary solution corresponding to thermal equilibrium (Spitzer 1942; Camm 1950; Rybicki 1971) as

$$f_S(x, v) = \frac{\rho_S}{[\operatorname{ch}(\sqrt{2\pi\rho_S/\sigma_S}x)]^2} \exp\left[-\frac{1}{2}\left(\frac{v}{\sigma_S}\right)^2\right]. \tag{A4}$$

Table A1. The designation of the simulations according to the important parameters used to perform them: type of initial conditions, refinement/unrefinement criteria parameters introduced in Section 2.2.3 (equations 12–15) and the time-step parameter C introduced in Section 2.2.4 (equation 16).

Designation	Initial conditions	S_{add}	S_{rem}	d_{add}	d_{rem}	C
Gaussian10U	Gaussian, 10 contours, unrefinement allowed	10^{-8}	$S_{\text{add}}/2$	0.01	0.005	0.025
Gaussian10	Gaussian, 10 contours, no unrefinement, larger S_{add}	2×10^{-8}	0	0.01	0	0.025
Gaussian84U	Gaussian, 84 contours, unrefinement allowed	10^{-8}	$S_{\text{add}}/2$	0.01	0.005	0.025
Gaussian84	Gaussian, 84 contours, no unrefinement, larger S_{add}	2×10^{-8}	0	0.01	0	0.025
RandomU	Random set of haloes, unrefinement allowed	10^{-8}	$S_{\text{add}}/2$	0.01	0.005	0.005
Random	Random set of haloes, nonrefinement, larger S_{add}	2×10^{-8}	0	0.01	0	0.005
RandomUT	Random set of haloes, unrefinement allowed, smaller time step	10^{-8}	$S_{\text{add}}/2$	0.01	0.005	0.0025
RandomUS	Random set of haloes, unrefinement allowed, smaller S_{add}	10^{-9}	$S_{\text{add}}/2$	0.01	0.005	0.005
Tophat1.000U	Waterbag, $\Delta p = 1$, unrefinement allowed	10^{-7}	$S_{\text{add}}/2$	0.02	0.01	0.0025
Tophat0.750U	Waterbag, $\Delta p = 0.75$, unrefinement allowed	0.75×10^{-7}	$S_{\text{add}}/2$	0.02	0.01	0.0025
Tophat0.500U	Waterbag, $\Delta p = 0.5$, unrefinement allowed	0.5×10^{-7}	$S_{\text{add}}/2$	0.02	0.01	0.0025
Tophat0.250U	Waterbag, $\Delta p = 0.25$, unrefinement allowed	0.25×10^{-7}	$S_{\text{add}}/2$	0.02	0.01	0.0025
Tophat0.100U	Waterbag, $\Delta p = 0.1$, unrefinement allowed	10^{-8}	$S_{\text{add}}/2$	0.02	0.01	0.0025
Tophat0.010U	Waterbag, $\Delta p = 0.01$, unrefinement allowed	10^{-9}	$S_{\text{add}}/2$	0.02	0.01	0.0025
Tophat0.010	Waterbag, $\Delta p = 0.01$, no unrefinement, larger S_{add}	10^{-9}	$S_{\text{add}}/2$	0.02	0.01	0.0025
Tophat0.003U	Waterbag, $\Delta p = 0.003$, unrefinement allowed	0.3×10^{-9}	$S_{\text{add}}/2$	0.02	0.01	0.001
Tophat0.003	Waterbag, $\Delta p = 0.003$, no unrefinement, larger S_{add}	2.4×10^{-9}	0	0.02	0	0.001
Tophat0.001U	Waterbag, $\Delta p = 0.001$, unrefinement allowed	10^{-10}	$S_{\text{add}}/2$	0.02	0.01	0.001
Tophat0.001	Waterbag, $\Delta p = 0.001$, no unrefinement, larger S_{add}	8×10^{-10}	0	0.02	0	0.001
Tophat0.001S	Waterbag, $\Delta p = 0.001$, no unrefinement	10^{-10}	0	0.02	0	0.001
PerturbedU	Waterbag, $\Delta p = 0.003$, perturbed, unrefinement allowed	10^{-10}	$S_{\text{add}}/2$	0.02	0.01	0.0005
Perturbed	Waterbag, $\Delta p = 0.003$, perturbed, no unrefinement, larger S_{add}	8×10^{-10}	0	0.02	0	0.0005
PerturbedS	Waterbag, $\Delta p = 0.003$, perturbed, no unrefinement	10^{-10}	0	0.02	0	0.0005

The individual components are generated at random positions in a phase-space disc of radius unity (prior to recasting with respect to centre-of-mass). Their profile follows equation (A4) with $\rho_S = 6$ and individual random values for the velocity dispersion σ_S , ranging in the interval $[0.005, 0.1]$. To make sure that the clouds do not overlap too much with each other, we impose the distance in phase-space between the centre of any two clouds i and j to be larger than $4[\sigma_S(i) + \sigma_S(j)]$. Then, the components are added on the top of each other in phase-space, to obtain the desired distribution function $f_i(x, v)$. Finally, apodization is performed as follows.

$$f(x, v) = f_i(x, v), \quad f_i(x, v) \geq \eta_r, \quad (\text{A5})$$

$$= \eta_r \max \left\{ 1 + 2 \operatorname{th} \left[\frac{f_i(x, v) - \eta_r}{\eta_r} \right], 0 \right\},$$

$$f_i(x, v) < \eta_r, \quad (\text{A6})$$

with $\eta_r = 0.05$.

(iii) Our single-waterbag simulations have the following initial vertices coordinates for the orientated polygon:

$$x_i = \cos(2\pi i/N), \quad (\text{A7})$$

$$v_i = \Delta p \sin(2\pi i/N), \quad (\text{A8})$$

with $i \in [0, \dots, N]$ and a total mass unity, which implies $f^{\text{left}} = 1/(\pi \Delta p)$ and $f^{\text{right}} = 0$ in equation (9). As listed in Table A1, we consider several values of the thickness parameter Δp ranging in the interval $[0.001, 0.1]$. In all the cases, we take $N = 1000$.

For $\Delta p = 0.003$, we also performed simulations where the initial configuration is perturbed randomly as follows.

$$v \rightarrow v + \delta v, \quad (\text{A9})$$

$$\delta v = 0.0006 \sum_{k=-50}^{50} |k|^{-1/2} [G_{2k} \cos(\pi k x) + G_{2k+1} \sin(\pi k x)], \quad (\text{A10})$$

where G_i is a Gaussian random number of average zero and variance unity. In this case, we take $N = 10\,000$.

The simulations were run up to $t = 50$, except for the perturbed waterbag simulations which ended earlier, due to their computational cost.

SUPPORTING INFORMATION

Additional Supporting Information may be found in the online version of this article:

Appendix B: Initial Conditions with the Isocontour Method

Appendix C: Details on Refinement

Appendix D: Details on the Calculation of the Time Step

Appendix E: Tests on Energy Conservation

Appendix F: Circulation along the Orientated Polygon

Appendix G: Position-Velocity to Action-Angle Transformation

Appendix H: Phase-Space Energy Distribution Function

Appendix I: Drawing Waterbags

Appendix J: Lagrangian Perturbation Theory

(<http://mnras.oxfordjournals.org/lookup/suppl/doi:10.1093/mnras/stu739/-/DC1>).

Please note: Oxford University Press is not responsible for the content or functionality of any supporting materials supplied by the authors. Any queries (other than missing material) should be directed to the corresponding author for the article.

This paper has been typeset from a $\text{\TeX}/\text{\LaTeX}$ file prepared by the author.